

Dynamic Forcing Behind Hurricane Lidia's Rapid Intensification

Mauricio López-Reyes^{1,2,3}, María Luisa Martín^{4,5}, Carlos Calvo-Sancho^{4,6}, Juan Jesús González-Alemán⁷

¹Instituto de Astronomía y Meteorología (IAM), Centro Universitario de Ciencias Exactas e Ingenierías (CUCEI), Departamento de Física, Universidad de Guadalajara, Guadalajara, Mexico.

²Department of Earth Physics and Astrophysics, Faculty of Physics, Complutense University of Madrid, Madrid, Spain.

³Instituto Frontera A.C., Departamento de Investigación, Tijuana, México.

⁴Department of Applied Mathematics, Faculty of Computer Engineering, University of Valladolid, Spain.

⁵Institute of Interdisciplinary Mathematics (IMI), Complutense University of Madrid, Madrid, Spain.

⁶Centro de Investigaciones sobre Desertificación, Consejo Superior de Investigaciones Científicas (CIDE, CSIC-UV-Generalitat Valenciana), Climate, Atmosphere and Ocean Laboratory (Climatoc-Lab), Moncada, Valencia, Spain

⁷Department of Development and Applications, Agencia Estatal de Meteorología (AEMET), Madrid, Spain.

Corresponding author: C. Calvo-Sancho (carlos.calvo@csic.es)

Key words

Rapid intensification, ensemble prediction, tropical cyclone, extratropical interactions

Key points

- A mid-to-upper level trough enhanced vertical motion and divergence over Hurricane Lidia, triggering rapid intensification.
- Stronger Trenberth forcing, eddy flux convergence, and vorticity advection were observed in ensemble members that captured RI.
- Ensemble diagnostics revealed that dynamic forcing preceded RI onset, suggesting a causal role beyond thermodynamic conditions.

Abstract

This study examines Hurricane Lidia's rapid intensification (RI) in the understudied northeastern Pacific, focusing on its interaction with an upper-level trough. Using IFS-ECMWF ensemble forecasts and ERA5 reanalysis, we analyze the large-scale dynamical mechanisms driving Lidia's intensification. Results show that the trough played a crucial role in promoting RI by enhancing synoptic-scale ascent, upper-level divergence, and eddy flux

convergence. In the higher-intensification ensemble group, a coherent sequence emerged in which enhanced negative Trenberth forcing appeared several hours before RI onset, followed by marked increases in upper-level divergence, cyclonic vorticity advection, and mid-tropospheric moistening. These signals collectively reduced vertical wind shear over the storm and strengthened the upper-level outflow, creating an environment highly conducive to RI. In contrast, the lower-intensification group exhibited weaker forcing, higher shear, and a lack of sustained divergence in upper levels. These findings highlight the importance of diagnosing early dynamical triggers for RI, particularly in regions where operational access to high-resolution models is limited. A conceptual schematic synthesizes these multi-stage processes, highlighting how upper-level dynamical forcing and favorable thermodynamic conditions acted jointly to precondition and then accelerate RI. This approach provides a cost-effective framework for anticipating RI using ensemble-based diagnostics and could serve as a valuable forecasting tool in data-sparse areas such as the Pacific coast of Mexico. Future studies should combine this large-scale methodology with high-resolution simulations to better capture storm-scale processes and validate multi-scale interactions in RI events.

1 Introduction

México is among the countries most affected by tropical cyclones (TCs) from both the Atlantic and Pacific Oceans (Larson et al., 2005; López-Reyes et al., 2024). While the Atlantic basin has traditionally garnered more research attention, largely due to the severe economic and social impacts of TCs in the United States, there is a pressing need to expand research efforts in the northeastern Pacific basin, where fewer studies have been conducted (García Franco et al., 2024). In recent years, various major hurricanes, such as Patricia, Lidia, and Otis caused large economic losses and scores of deaths in México (Pasch, 2024; García Franco et al., 2024). These events also posed challenges for numerical weather prediction models, particularly in forecasting their tracks and intensification processes. As highlighted by Shi and Chen (2021), one of the key obstacles is improving the prediction of TCs that undergo rapid intensification (RI), defined as an increase of at least 30 kt (≈ 54 km/h) in maximum sustained wind speed within a 24-h period (Kaplan and DeMaria, 2003). Recent studies have shown a rise in the frequency of RI events in the Atlantic basin, driven primarily by ocean warming (Majumdar et al., 2023; Li et al., 2023). The northeastern Pacific, however, has also experienced extreme intensification rates, with Patricia (2015), Willa (2018), and Otis (2023) ranking among the most rapidly intensifying storms on record. Similarly, during the 2024 hurricane season, Hurricane Milton underwent explosive intensification, posing a significant challenge for intensity forecasting (Pasch, 2024). Enhancing our ability to forecast RI is essential for reducing the risk these powerful storms pose to vulnerable communities and critical infrastructure.

Although RI is strongly influenced by thermodynamic factors, such as high sea surface temperatures (SSTs) and ocean heat content, dynamic factors also play a pivotal role. Interactions between TCs and upper-level troughs have been shown to significantly affect storm intensity (Fischer et al., 2019). According to Avila (1998), Hanley et al. (2001), López-Reyes et al. (2021) and DeMaria et al. (2021), forecasting intensity changes in TCs remains one of the biggest challenges, particularly during RI. The difficulties in forecasting RI stem from the complex factors involved in the occurrence of RI, such as the large-scale environment, internal dynamics and multiscale interactions (Kaplan et al., 2010; Zhang and Chen 2012; 2020; Wang et al., 2021; Shi and Chen 2021). Over the past few years, there has been notable progress in understanding the internal dynamics that govern RI. As found in Chen et al. (2019) and Shi and Chen (2021), key internal dynamical and thermodynamic features associated with RI include strong upper-level divergence and strong boundary-layer convergence as well as a weak deep-layer vertical wind shear (VWS), higher relative humidity throughout the vertical column, and high intensification potential (details in Emanuel, 1988) associated with SST. Other studies have highlighted the significance of the deep convective region surrounding the eyewall and the large convergence of angular momentum into TC (Stevenson et al., 2014; Komaromi and Doyle 2018; Ryglicki et al., 2021).

While these internal mechanisms are primary to the intensification process, the surrounding environment can modulate RI by providing dynamically favorable conditions, such as upper-level forcing or favorable trough interactions. From a kinematic perspective,

however, changes in intensity ultimately result from the TC's ability to evacuate mass from the boundary layer through convection and draw in angular momentum, as recently emphasized by Montgomery and Smith (2025) and Smith et al. (2021). Furthermore, research studies have identified a relevant relationship between the structure and size of TCs, their environmental conditions, and the TC intensification rate (Carrasco et al., 2014; Shi and Chen 2019; Tao et al., 2022; Ston et al., 2023; Nayaranan et al., 2024).

Since the general conditions favoring TC RI are well-known, other factors may influence the overall intensification processes. In a follow-up theoretical study, Leroux et al. (2016) identified an optimal TC-trough alignment that promotes interaction (Komaromi and Doyle 2018; Shato et al., 2020). Similarly, studies by DeMaria et al. (1993), Hanley et al. (2001), and Peirano et al. (2016) suggest that an approaching upper-tropospheric trough can play a critical role in hurricane intensification. However, trough interactions can also limit TC intensification, depending on the configuration of the trough and its associated jet stream. For example, increased dry air entrainment or increased VWS can inhibit TC development (Peirano et al., 2016). Recent research has identified specific synoptic configurations that favor RI, including short zonal wavelengths and favorable upstream displacements between the TC and the trough (Fischer et al., 2019). Qiu et al. (2020) also showed how important eddy flux convergence (EFC) is for identifying trough interactions, particularly when large-scale circulation patterns favor stronger upper-level divergence. In the same way, Yan et al. (2021) found that upper-tropospheric cold lows could enhance EFC, reduce inertial stability, and strengthen upper-level divergence, leading to RI. These studies show that TC-trough interactions can have two effects and stress how important it is to figure out what environmental conditions make TCs stronger or weaker.

Although TC–trough interactions have been extensively studied in the Atlantic basin, the northeastern Pacific remains understudied. During El Niño events, the subtropical Pacific warms considerably, increasing the likelihood of interactions between TCs and the jet stream, increasing the likelihood of dynamic interactions (Luna-Niño et al., 2021; Ling et al., 2024). On the other hand, these interactions often occur at higher latitudes over less populated areas in the Atlantic basin. In contrast, TCs in the northeastern Pacific tend to curve toward land, which puts densely populated areas in Mexico at risk. The fact that warm SSTs and the jet stream interact during El Niño events shows how important it is to do focused research in this area.

The most intense hurricanes that have affected Mexico typically occur during late summer and early autumn, as was the case with Hurricane Lidia in mid-October 2023. The devastating case of Hurricane Otis in October 2023, in which all global models failed to capture its RI, underscored the urgent need for improved understanding of RI processes in this region. Hurricane Lidia underwent an unusual RI just off the Pacific coast of Mexico in October 2023, surprising forecasters and resulting in widespread damage. Despite the proximity to land and under moderate VWS, the storm rapidly intensified and made landfall as a Category 4 hurricane (Pasch, 2024). The failure of operational models to predict this intensification (as in the case of Hurricane Otis the same month) underscores the urgent

need to improve the understanding the dynamical processes involved in such cases. Additionally, the proximity of northeastern Pacific TCs to mountainous terrain introduces further challenges for forecasting (DiMego et al., 1976). This event caused dozens of fatalities and severe and widespread damages in Acapulco, highlighting Mexico's vulnerability to such phenomena and the critical need for better forecast capabilities (Servicio Meteorológico Nacional, 2023; Emanuel, 2024). Given the high SSTs during this season, trough-TC interaction is particularly relevant during October and November, as many TCs turn eastward during this period. This turning is influenced by the subtropical jet stream, typically positioned between 25°N and 35°N, especially during seasons when El Niño events are present (Luna-Niño et al., 2021; Tong et al., 2023). The jet stream may enhance interactions between midlatitude troughs TCs.

While the underlying dynamics of these interactions may be broadly similar across ocean basins, the eastern North Pacific exhibits unique characteristics that justify a focused investigation. In particular, the variability of the subtropical jet, often modulated by ENSO (Liu et al., 2024), differs from typical Atlantic configurations (Zhao and Raga, 2015; Winters and Attard, 2022), and the recurving behavior of TCs toward the Mexican coastline during late-season months creates a distinct synoptic context. To the authors' knowledge, no previous studies have specifically investigated the role of the jet stream in TC RI in the northeastern Pacific. In contrast to most prior studies in the Atlantic basin, which primarily focus on thermodynamic drivers, our research emphasizes the dynamical forcing mechanisms relevant to the eastern North Pacific, particularly those associated with trough–TC interactions, such as quasi-geostrophic (QG) ascent, EFC, and enhanced upper-level divergence in the intensification of Hurricane Lidia. By analyzing ensemble prediction system (EPS) outputs and ERA5 reanalysis data, we provide a comprehensive assessment of the conditions that favored Lidia's RI, offering novel insights into the dynamics of TC intensification in the northeastern Pacific.

While operational mesoscale models such as the Hurricane Analysis and Forecast System (HAFS) now provide high-resolution forecasts for TCs in the eastern North Pacific, ensemble prediction systems (EPS) like those from the European Centre for Medium-Range Weather Forecasts (ECMWF) offer publicly accessible data and have demonstrated strong skill in capturing the uncertainty associated with complex and potentially high-impact TC scenarios. Therefore, ensemble-based diagnostics remain a valuable and scalable approach for assessing TC behavior and RI risks, particularly in resource-constrained forecasting environments such as Mexico.

This paper is organized as follows: Section 2 presents the data models and methods, including the ensemble configurations and diagnostics tools. Section 3 describes the synoptic conditions that influenced Hurricane Lidia's RI and discusses the main dynamical processes involved; a conceptual schematic summarizing these processes is also presented. Finally, Section 4 provides a summary of findings and concluding remarks.

2 Data Models and Methods

The data sets are based on forecasts from the Integrated Forecasting System (IFS) of the ECMWF. This study uses the operational perturbed forecast ensemble generated by the EPS (Cycle 48r1: ECMWF, 2023) with 50 perturbed members. Each perturbed member has a horizontal resolution of 0.1° and 137 vertical levels. The last initialization is selected since it features a large spread of Hurricane Lidia trajectories, corresponding to the October 8th, 00:00 UTC initialization, which spans a 96-hour forecast window with 1 h time steps. Additionally, to assess the performance of each composite group, key atmospheric fields are computed using data from the ERA5 climate reanalysis (Hersbach et al., 2020) with 0.25° horizontal resolution and 37 vertical levels, during the period with the highest intensification rate.

Several dynamic and thermodynamic variables were utilized in this study, such as mean sea level pressure (*MSLP*), temperature (*T*), geopotential height (*Z*), zonal and meridional wind components (*u, v*), potential temperature (θ), SST and relative humidity (*RH*). See Table 1 for additional details. To evaluate the role of the trough in the trajectory and intensity change of Hurricane Lidia we analyzed trajectories and intensification rate for all members using MSLP and grouped into two intensification rate groups (IRGs) based on the P_{20} (lower intensification rate) and P_{80} (highest intensification rate) percentiles of MSLP. These percentiles were calculated using the minimum central pressure attained by each ensemble member during the 24 h period of most rapid intensification (October 9, 00:00 UTC to October 10, 00:00 UTC) and were cross-validated using the maximum sustained wind speed to ensure that they met the official RI definition (greater than 54 km h^{-1} in 24 h). The NHC best track and official intensity data were used for comparison with both groups. As is common in studies of this nature (Chen et al., 2019; Chen et al., 2021; Hu and Zou, 2021; Collins et al., 2022), synoptic and storm-centered composites (SCC) are derived for the specified fields within a circular area with an 8° radius.

Table 1. Details on the atmospheric variables used.

Variable	Symbol	Pressure levels (PVU)	Units
Mean sea level pressure	<i>MSLP</i>	Surface	<i>hPa</i>
Temperature	<i>T</i>	Surface, 1000, 925, 850, 700, 500, 400, 300, 250, 200	<i>K</i>
Geopotential height	<i>Z</i>	1000, 925, 850, 700, 500, 400, 300, 250, 200	<i>m</i>
Zonal wind component	<i>u</i>	850, 300, 200	ms^{-1}
Meridional wind component	<i>v</i>	850, 300, 200	ms^{-1}
Potential temperature	θ	(1.5-PVU)	<i>K</i>
Sea surface temperature	<i>SST</i>	Surface	<i>K</i>
Relative humidity	<i>RH</i>	500 hPa	%

Based on the previous variables, some derived fields related with TC intensity change (Chen et al., 2021; Mei and Yu 2016) are also computed: VWS calculated between 850 and

200 hPa , between 0-500 km radius, irrotational wind (\vec{V}_{irr}) at 200 hPa, based on Helmholtz decomposition (details in Chorin et al., 1990 and Cao et al., 2014) and vorticity advection, $\vec{V} \cdot \nabla(\vec{\xi} + f)$ at 500 hPa, where $\vec{\xi} = \frac{\partial v}{\partial x} - \frac{\partial u}{\partial y}$ and f is the planetary vorticity.

Following Bister and Emanuel (1998) and Gilford (2021), potential intensity (PI) is also calculated as

$$PI = V_{max} = \left[\frac{C_k (T_s - T_0)}{C_D T_0} (h_s^* - h^*) \right]^{1/2},$$

where C_k is the enthalpy surface exchange coefficient, C_D is the momentum surface exchange coefficient, h_s^* is the saturation moist static energy at the sea surface, h^* is the saturation moist static energy of the air above the boundary layer, following to Wing et al. (2015), evaluated at 500-600 hPa. As mentioned in Gilford (2021), tropical cyclone thermodynamic disequilibrium and efficiency were represented by terms $(h_0^* - h^*)$ and $\frac{T_s - T_0}{T_0}$, where T_s is the sea surface temperature and T_0 is the outflow temperature level.

To identify regions that favor ascending air movements driven by synoptic-scale dynamical forcing associated with extratropical systems (Loughe et al., 1995; Hanley et al., 2001), ageostrophic wind (\vec{V}_{ag}) and its divergence ($\nabla \cdot \vec{V}_{ag}$) are additionally computed. The QG omega equation is also used to identify the synoptic ascent flow via Trenberth form (Billingsley, 1998; Bracken and Bosart, 2000). Trenberth QG forcing (Q) is calculated using the following expression

$$Q = \left(\sigma \nabla_p^2 + f_0^2 \frac{\partial^2}{\partial p^2} \right) \omega \approx 2 \left[f_0 \frac{\partial \vec{V}_g}{\partial p} \cdot \nabla \left(\frac{\partial v}{\partial x} - \frac{\partial u}{\partial y} + f \right) \right], \quad (1)$$

i.e., vertical air movements are proportional to advection by vorticity by thermal wind. Herein, σ is the stability parameter, f_0 the Coriolis parameter, ω the vertical component of wind ($Pa \cdot s^{-1}$), \vec{V}_g the geostrophic wind vector ($m s^{-1}$), p the pressure (Pa). To minimize the influence of small-scale noise and mesoscale features in the diagnostic fields, a spatial Gaussian filter ($\sigma = 1.5^\circ$) was first applied uniformly to the entire domain, preserving the synoptic-scale variability. In addition, to reduce potential contamination from the TC's own circulation, an additional localized Gaussian filtering was applied to the Q dynamical forcing fields within an 800 km radius centered on the storm, with a smooth cosine taper toward the surrounding environment. This procedure effectively attenuates the contribution of the TC's inner-core vorticity while maintaining the continuity and coherence of the synoptic-scale trough and jet stream features.

Finally, with the aim of measuring the degree of interaction between the trough and the TC, and following previous studies in the Atlantic Ocean (Molinari and Vollaro, 1990; Hanley et al., 2000; Komaromi and Doyle, 2018), the eddy flux convergence (EFC) is defined as

$$EFC = -\frac{1}{r^2} \frac{\partial}{\partial r} (r^2 \overline{v_r' v_t'}), \quad (2)$$

where v_r' is the perturbation radial wind, v_t' the perturbation tangential wind, and the overbar denotes the azimuthal mean, computed in storm-relative coordinates. Based on the methodology of DeMaria et al. (1993) and Hanley et al. (2001), the EFC is computed over a radial range of 300 to 600 km for each time step during RI period. The calculation spans the full 96 h forecast period starting from the model initialization, thereby encompassing pre-RI, RI, and post-RI phases for both ERA5 and members groups.

To compare atmospheric fields between the most and least intensifying groups, averages and standard deviations (STD) are calculated, and ensemble difference spatial distributions ($P_{80} - P_{20}$) are generated to visualize the contrasts between the two groups. In addition, time series of means and STDs of the thermodynamic and dynamic variables analyzed between the groups during the simulation period are performed. Finally, a Mann-Whitney U test is performed to identify regions with statistically significant differences at the 95% confidence level (Mann and Whitney, 1947).

3 Results

3.1 Trajectory and intensity forecast analysis.

Hurricane Lidia originated from a tropical wave on 3 October 2023 (Pasch, 2024). Between 3 and 5 October, it remained a disorganized system, marked by significant uncertainty in both track and intensity forecasts (Figures S1). From 5 to 7 October, Lidia generally tracked westward under the influence of a mid-level ridge but remained poorly organized. By 8 October, the subtropical jet stream was positioned between 20° and 30°N, aligned with Lidia's latitude (Figures A1 and 2 in Appendix). At this stage, a mid-to-upper-level trough approaching the Baja California Peninsula began to influence Lidia's motion, steering the system northward and subsequently eastward.

At approximately 18:00 UTC on 9 October, Lidia entered a phase of intensification (Pasch, 2024). This intensification was accompanied by a northeastward turn induced by an approaching trough from the northwest, although considerable spread in forecast trajectories persisted at this time (Fig. 1a). On 10 October, Lidia underwent RI, with maximum sustained winds increasing by 82 km h^{-1} over an 18-hour period, ultimately reaching a peak intensity of nearly 220 km h^{-1} . This placed Lidia at Category 4 on the Saffir–Simpson Hurricane Wind Scale.

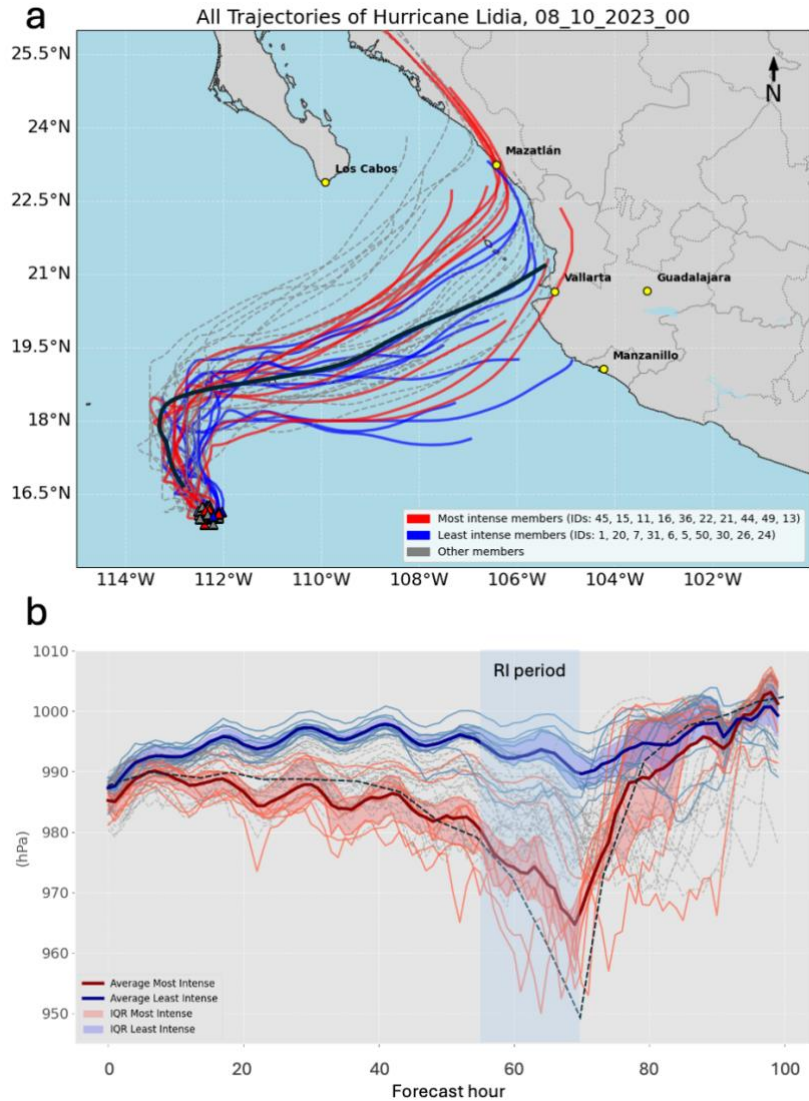


Figure 1. (a) Lidia’s Trajectories for all members, highest (lower) IRG in red (blue) line and best track of NHC (black line). (b) Intensity temporal evolution for all members (MSLP), highest (lower) IRG in red (blue) line, shaded areas correspond with interquartile range; official MSLP in black dotted line.

Figure 1a shows the trajectories of Hurricane Lidia’s ensemble members from the ECMWF, initialized at 00:00 UTC on 8 October. The trajectories of the most intense members are positioned further north relative to those of the lower-intensity members, relative to the NHC best track. This suggests that the trough’s proximity influenced event predictability, increasing uncertainty in both track and intensity forecasts (Figures A1 and 2 in Appendix). This pattern aligns with findings from Ito and Wu (2013), Callaghan (2020), and Sato et al. (2020) in the Atlantic basin, indicating the contribution of synoptic environment to the low predictability of both trajectory and intensity of the cyclone, as here evidenced by the large spread in Figures 1a, b. Furthermore, based on the temporal evolution of Lidia’s MSLP and

wind speed (Fig. 1b), seven members in the P_{80} -ensemble group, along with the ensemble mean, successfully simulate Lidia's rapid intensification, exceeding the RI threshold.

As is well known and formulated in the Emanuel model (Emanuel, 2002) and used in Chen et al. (2021), the oceanic and atmospheric variables such as T_s , T_0 and saturation parameters (eq. 1), determine the PI that the TC could acquire. Both ensembles display similar PI distributions around Hurricane Lidia (Figs. 2a, b). However, somewhat unexpectedly the P_{20} -ensemble shows a higher PI value ($\sim 250 \text{ km h}^{-1}$) compared to the P_{80} -ensemble ($\sim 240 \text{ km h}^{-1}$), although the differences are not statistically significant (not shown).

Based on the PI time series (Fig. 2c), this diagnostic variable alone does not appear to support Lidia's RI. Therefore, this suggests that thermodynamic factors are necessary but not sufficient to trigger RI. This finding is consistent with recent studies (e.g., Gilford, 2021; Shi and Chen, 2021) which suggest that while PI provides an upper bound, the actual intensification process is modulated by environmental dynamics, including ventilation and vertical motion induced by synoptic-scale features such as upper-level troughs. These results highlight the potential value of ensemble forecasts for anticipating RI events under favorable environmental and synoptic conditions. In the following sections, we examine the temporal evolution and structural characteristics of the large-scale dynamical forcing, including the trough interaction, to support this interpretation.

Similarly, the spatial SST differences between the P_{80} - and P_{20} -ensembles (Fig. 3a–f) reinforce the conclusion that thermodynamic conditions alone do not explain the contrasting intensification outcomes. While some localized differences exceeding $\pm 5^\circ\text{C}$ appear at specific time steps, these do not persist or align consistently with the RI period. The warm anomalies observed in the P_{20} -ensemble are mainly displaced to the north and northeast of Lidia's core. This spatial misalignment suggests that, despite slightly warmer SSTs, the coupling between oceanic energy supply and inner-core dynamics was likely suboptimal.

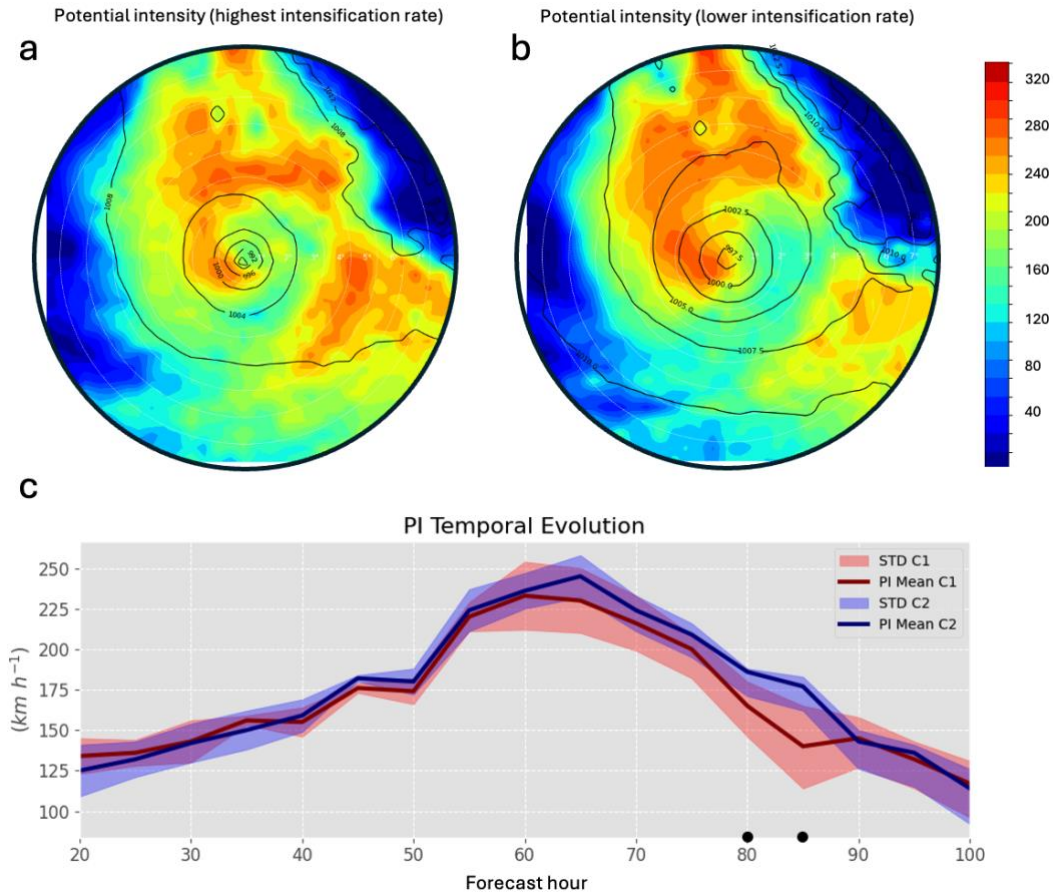


Figure 2. (a) Highest intensification rate PI SCC and (b) lower intensification rate PI SCC ($km\ h^{-1}$) at +55-h and (c) PI computed within a radial range of 6° , with the red (blue) line representing the higher (lower) IRG. The red (blue) shaded regions indicate the STD for the highest (lower) IRG.

Statistical significance markers confirm that most SST anomalies are not spatially coherent enough to produce systematic differences in PI. This is consistent with the similar PI fields seen in both ensembles (Figs. 2a, b) and the absence of a clear thermodynamic advantage during the intensification period. Therefore, these SST patterns likely played a secondary role compared to the dynamically driven processes, such as enhanced vorticity advection and upper-level divergence.

This supports the notion that SSTs, in this case, provided a necessary but not sufficient condition for RI. The findings from Bister and Emanuel (2002) and Fischer et al. (2019) reinforces this view by emphasizing that, without favorable upper-level forcing and adequate storm structure, warm SSTs alone are insufficient to trigger RI, even when PI values appear theoretically consistent.

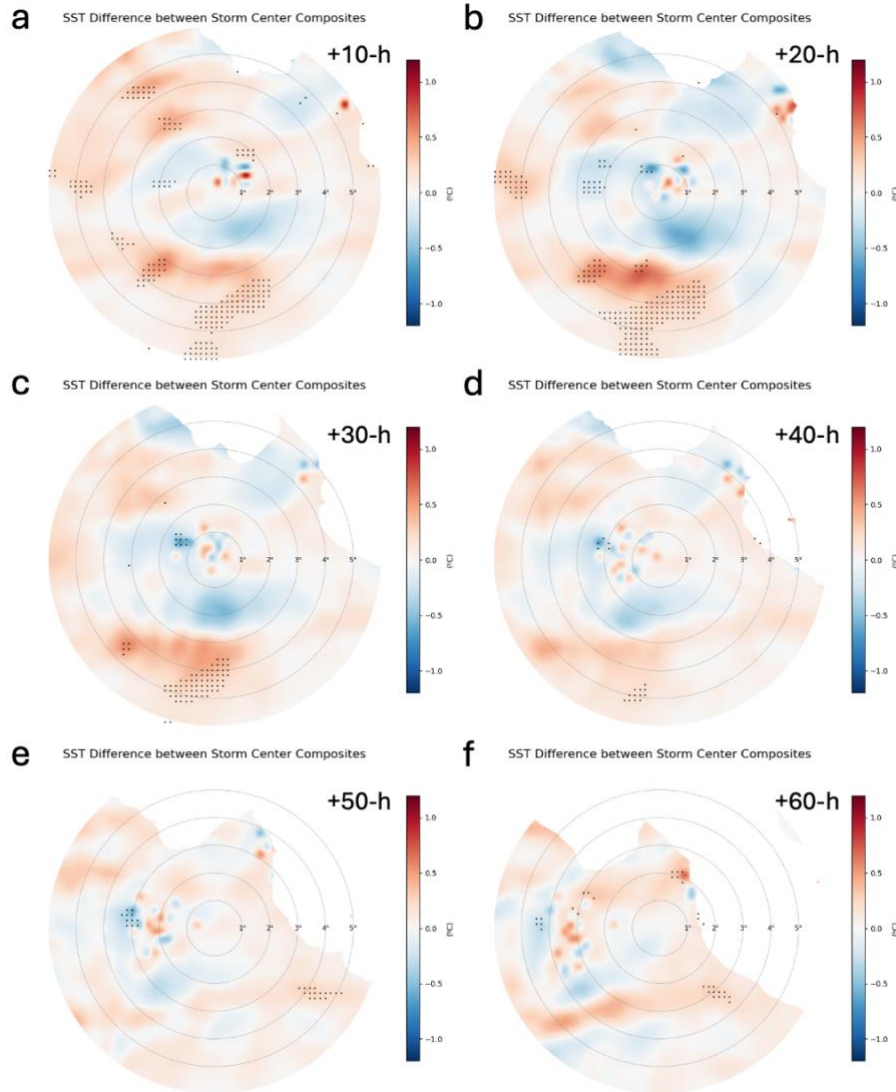


Figure 3. (a-f) SST SCC difference maps (P_{80} - P_{20} ensembles; °C) for selected time steps from +10 h to +60 h. Dots indicate regions where differences are statistically significant at the 95% confidence level.

3.2 Trough interaction and TC rapid intensification

Since SST fail to explain the differences observed among the ensemble members in Lidia's intensification, we examine the mid- and upper-level dynamic environment. Figure 4 shows the eastward progression of a trough in both ensemble groups. The trough is notably broader in the P_{80} -ensemble, particularly from time step +55 h. At 250 and 300 hPa (Figs. 4a, b), the isohypses in the P_{80} -ensemble exhibit substantial deformation toward Lidia. The trough deepens further at 500 hPa (Fig. 4c), extending southward to approximately 20°N. This southward intrusion brings the trough into closer proximity with the tropical cyclone, especially in the RI ensemble members, where a more pronounced elongation is observed.

This configuration likely favored a moist and unstable environment ahead of the cyclone, while simultaneously enhancing vorticity advection and synoptic-scale ascent.

Such a configuration is consistent with previous findings on optimal trough–tropical cyclone interactions (e.g., Hanley et al., 2001; Fischer et al., 2019), which suggest that intensification is favored when the trough approaches from the northwest at an appropriate distance. Although Fischer et al. (2019) noted that narrower upper-tropospheric troughs may be more conducive to RI, the enhanced interaction observed here may result from the deeper and more equatorward positioning of the broader trough in the RI group (particularly at +45 h and +55 h in Fig. 4c). Additionally, although our analysis focused primarily on dynamical variables, we acknowledge that mid-level tropospheric humidity, particularly the intrusion of dry air, may also have influenced the timing or suppression of RI in some ensemble members, as highlighted in recent work by Fischer et al. (2023). A more detailed analysis of the humidity and ventilation effects is presented in later sections.

The EFC is computed to diagnose the trough-TC interaction in Hurricane Lidia. The results indicate that P_{80} -ensemble exhibits significantly higher EFC values compared to the P_{20} -ensemble group. These differences begin to emerge around +40 h and become significant between +50 h and +80 h just before and during Lidia RI period (Fig. 5), suggesting that enhanced EFC may have contributed to the onset and maintenance of RI in the P_{80} members. P_{80} -ensemble is closely aligned with ERA5 reanalysis (exceeding $10 \text{ m s}^{-1} \text{ day}^{-1}$ during RI period). These elevated EFC values are consistent with the findings of DeMaria et al. (1993) for the North Atlantic basin, where EFC values greater than $10 \text{ m s}^{-1} \text{ day}^{-1}$ serve as an indicator of a trough-TC interaction. Therefore, the obtained EFC values highlight a strong interaction between Lidia and the trough, suggesting that dynamic forcing, estimated using a QG diagnostic framework, specifically the Trenberth formulation enhances vertical motion and may contribute to upper-level divergence, potentially triggering RI. This behavior in the Pacific is analogous to the quasi-stationary effect of the tropical upper tropospheric trough (TUTT) in the Caribbean, previously analyzed by Sanders (1975). However, unlike the Caribbean TUTT, which tends to be more persistent and conducive to cyclogenesis, the trough interacting with Hurricane Lidia in the Pacific was transient and engaged with an already mature TC. While we do not explore track changes in detail here, prior analyses suggested that this synoptic feature may have also influenced Lidia's trajectory in earlier initializations. Nonetheless, our focus remains on the intensification phase. These types of interactions are particularly relevant for hazard assessment, as they can increase the risk for densely populated areas in Mexico during late summer, when TCs are most frequent in the eastern Pacific basin (López-Reyes and Meulenert, 2021).

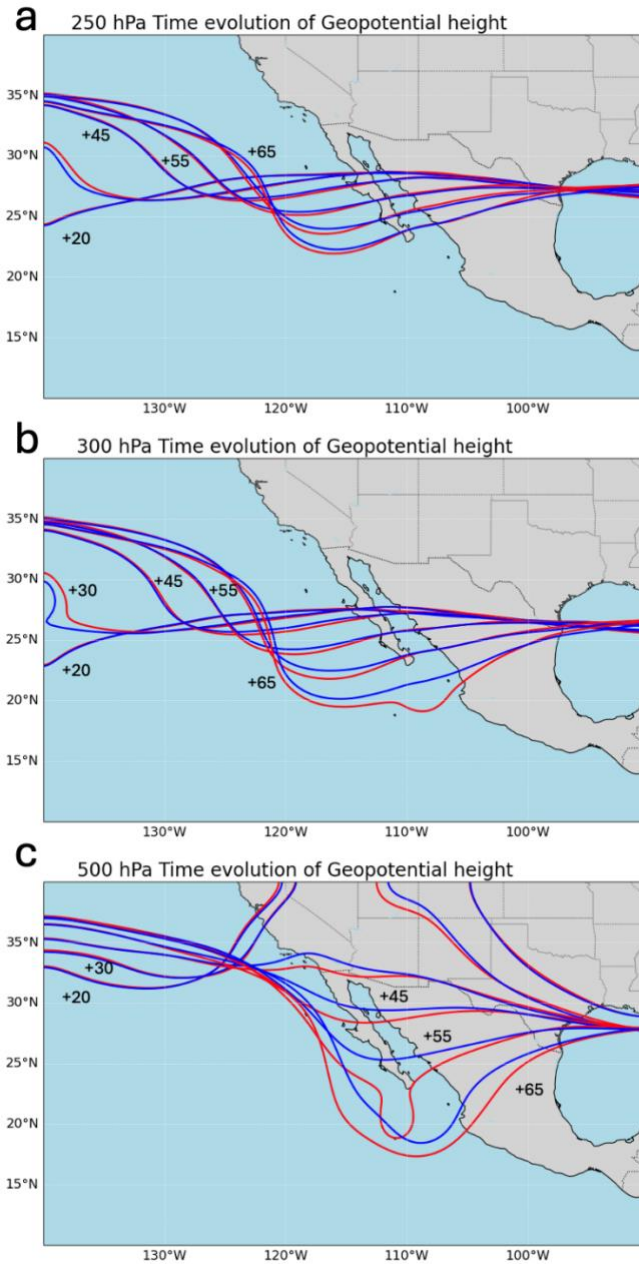


Figure 4. Z Composite corresponding to the highest (red contours) and lower (blue contours) IRG, at (a) 250 hPa, (b) 300 hPa and (c) 500 hPa, before and during the trough-TC interaction.

To assess the dynamical processes supporting Lidia's intensification, EPS outputs during the RI period are compared with ERA5 fields. Although quasi-geostrophic diagnostics are typically applied in extratropical contexts, this approach is particularly relevant in the northeastern Pacific, where the presence of the subtropical jet during the boreal autumn increases the likelihood of TC-subtropical jet stream (Hanley et al., 2001). These interactions can play a key role in TC intensification and recurvature, especially in a region where high-resolution forecasts remain limited.

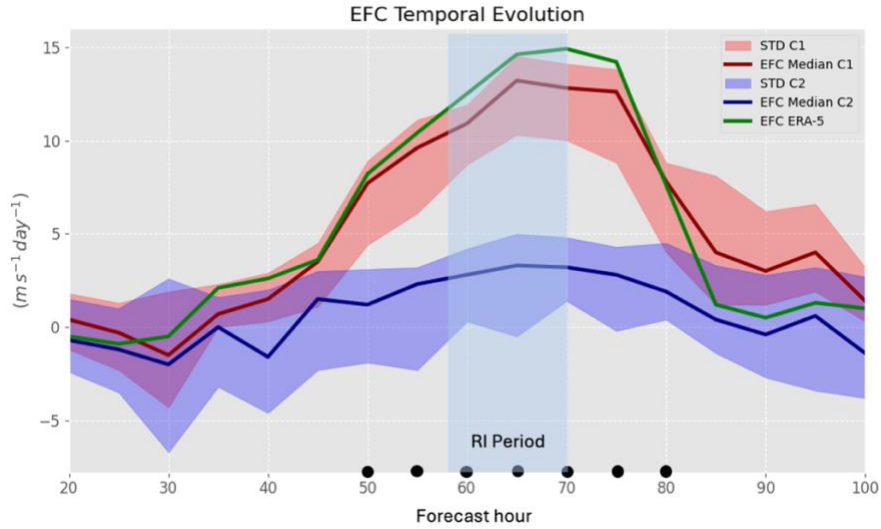


Figure 5. EFC temporal evolution calculated within a radial range of 300 to 600 km at 250 hPa, with the red (blue) line representing the higher (lower) IRG. The red (blue) shaded regions indicate the STD for the highest (lower) IRG, green line represents the EFC based on ERA5 data and dots indicate statistical significance.

In Figures 6a and 6b, the $\nabla \cdot \vec{V}_{ag} > 0$ values, associated with the trough and jet streak, are located to the northeast of Lidia. This configuration strongly favors enhanced upper-level divergence over Lidia and acts as a mechanism that drives upward motions. The quasi-geostrophic $\nabla \cdot \vec{V}_{ag}$ is notably higher in P_{80} than in P_{20} -ensemble (Fig. 6a-c); P_{80} -ensemble closely matches ERA5 across nearly all regions surrounding Lidia (Fig. 6d), suggesting a stronger forcing induced by the interaction with the trough and jet streak.

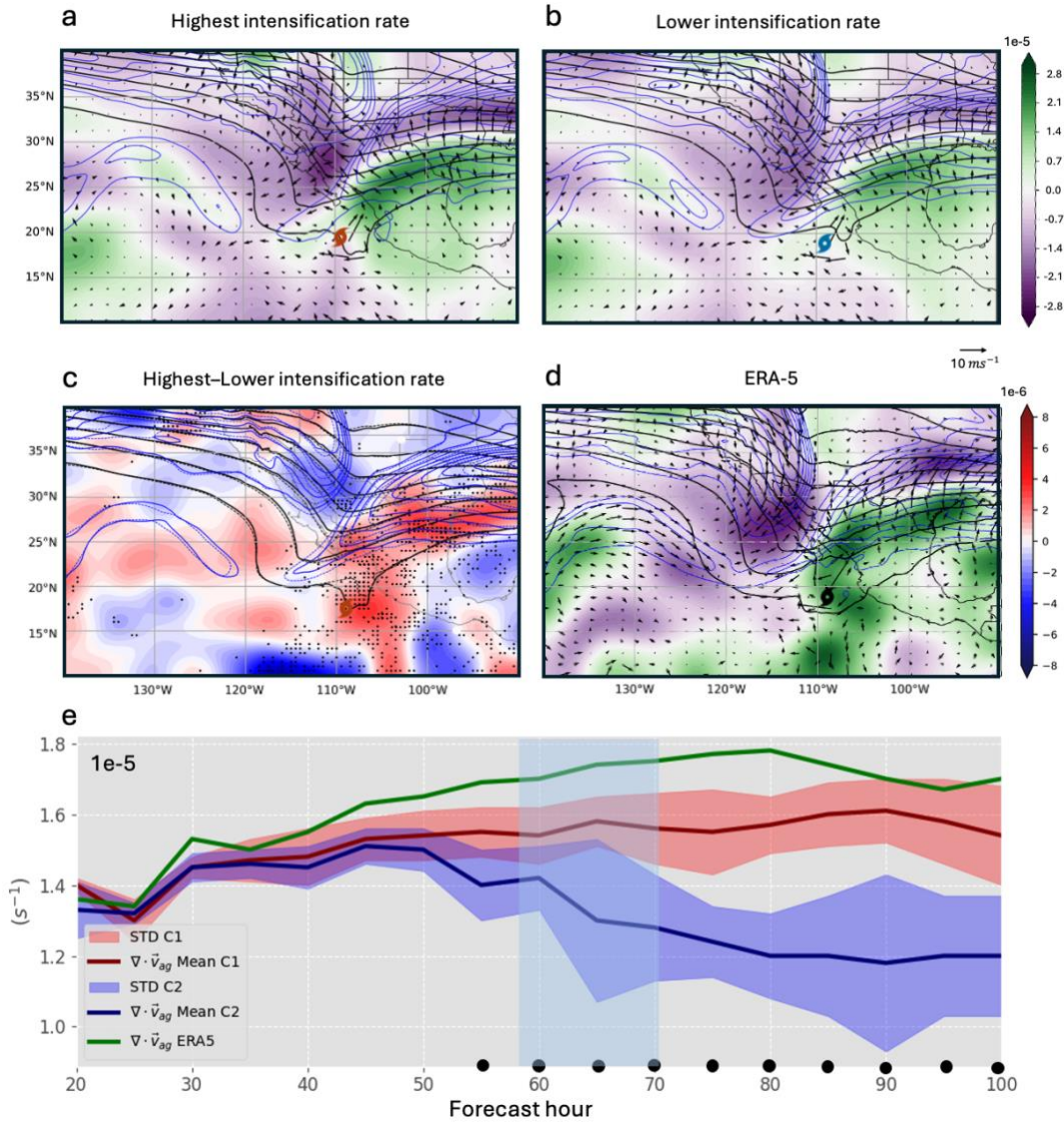


Figure 6. $\nabla \cdot \vec{V}_{ag}$ -Composite (shaded; s^{-1}), jet stream (blue contours at 10 ms^{-1} intervals) and Z at 250 hPa (black contours at 20 m intervals) of (a) P_{80} , (b) P_{20} IRG (c) $P_{80} - P_{20}$ of $\nabla \cdot \vec{V}_{ag}$ (shaded; dots indicated statistical significance), solid (dashed) contour represent Z of P_{80} (P_{20}) IRG, and (d) same for ERA5 data. e) $\nabla \cdot \vec{V}_{ag}$ Temporal evolution calculated within a radial range of 500 km at 250 hPa, with the red (blue) line representing the higher (lower) IRG. The red (blue) shaded regions indicate the STD for the highest (lower) IRG and dots indicate statistical significance.

Figure 6e reveals distinct differences in the evolution of ageostrophic divergence between the two ensemble groups. The P_{80} -ensemble shows consistently higher values of ageostrophic divergence, particularly between +50 and +75 h, coinciding with Lidia's RI period. In contrast, the P_{20} -ensemble exhibits lower and declining values during this period, indicating weaker dynamical forcing. ERA5 closely follows the P_{80} -ensemble pattern,

supporting the physical credibility of the ensemble signal. These results highlight the role of upper-level divergence and jet-induced ascent in supporting RI in the P_{80} -ensemble.

According to the quasi-geostrophic theory, regions with positive (negative) vorticity advection are associated with upward (downward) vertical motions (Bluestein, 1992). In Figures 7a and 7b, $\vec{V} \cdot \nabla(\vec{\xi} + f)$ is associated with a trough configuration, depicting predominant positive (negative) values in front (behind) of the trough axis. In the same way, $\vec{V} \cdot \nabla(\vec{\xi} + f)$ shows stronger and statistically significant positive values near Lidia's position in P_{80} compared to P_{20} -ensemble (Fig. 7c); in addition, a branch with positive vorticity advection values around Lidia is only identified in P_{80} -ensemble, and similar to ERA5 (Fig. 7d). The above is consistent with the greater proximity of the trough to Lidia in P_{80} -ensemble, highlighting a more intense cyclonic vorticity advection over Lidia (also at earlier time steps; not shown). However, we acknowledge that part of this signal also reflects the contribution from the TC circulation itself. Nonetheless, at the synoptic scale, coherent differences associated with the trough's position and structure are clearly discernible between ensemble groups. Therefore, the trough-TC interaction is more robust in P_{80} than in P_{20} as indicated earlier with the EFC metric. This finding shows that a mid- and upper-levels trough can facilitate the development of a moist layer (Wu et al., 2015), contributing to Lidia intensification.

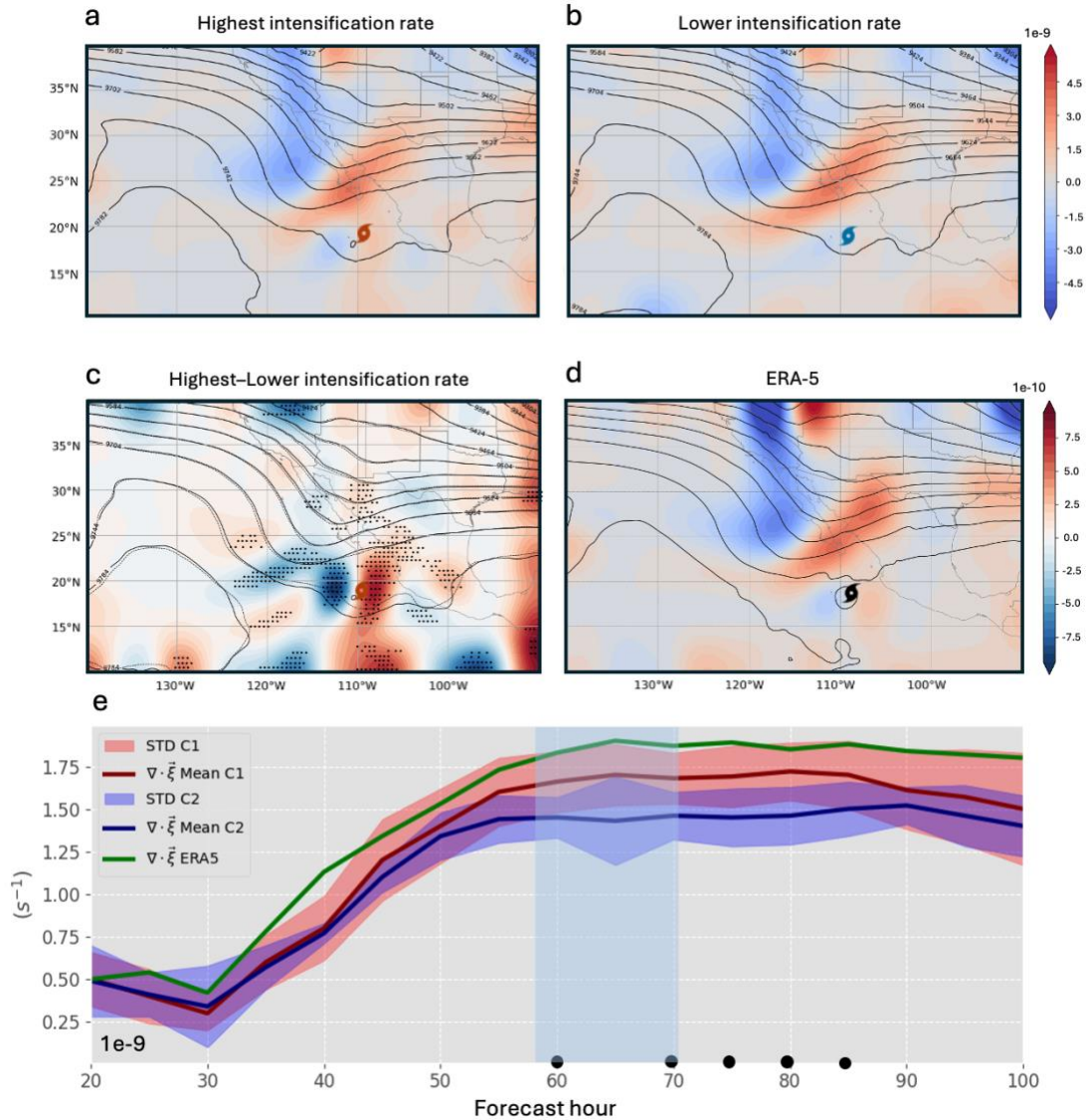


Figure 7. $\vec{V} \cdot \nabla(\xi + f)$ -Composite (shaded; s^{-2}) and Z at 300 hPa (black contours at 20 m intervals) of (a) the P_{80} (b) P_{20} IRG, (c) $P_{80} - P_{20}$ (shaded; dots indicated statistical significance), solid (dashed) contour represent Z of P_{80} (P_{20}) IRG and (d) same for ERA5 data. e) $\vec{V} \cdot \nabla(\xi + f)$ Temporal evolution calculated within a radial range of 500 km at 500 hPa, with the red (blue) line representing the higher (lower) IRG. The red (blue) shaded regions indicate the STD for the highest (lower) IRG and dots indicate statistical significance.

Figure 7e confirms the stronger vorticity forcing in the P_{80} -ensemble throughout Lidia's intensification period. From time step +40 h onward, the P_{80} group exhibits consistently higher values of vorticity advection, peaking near the RI window (+55 to +70 h), while the P_{20} group remains consistently weaker, with little variability. The ERA5 line again follows the P_{80} trajectory, supporting the robustness of the dynamical signal. The statistically significant differences suggest that enhanced cyclonic vorticity advection, likely associated with the trough's mid- and upper-levels deformation, played a crucial role in promoting upward motion and intensification in the P_{80} -ensemble.

The Q field in the P_{80} -ensemble (Fig. 8a) shows a more intense upward forcing in the right region of the trough and extending to the divergence zone at the right entrance of the jet streak in comparison to P_{20} Q values (Fig. 8b). We selected the 500 hPa level because this level exhibited stronger trough elongation and clearer interaction with the TC. This contrast becomes even more evident when considering only RI members within P_{80} -ensemble (Figs. 9 and Fig. A3 in Appendix) are selected and reinforces the idea of the influence of the trough in Lidia's RI. Based on Eq. (1), negative values of the forcing term Q correspond to regions of upward vertical motion induced by vorticity advection via the thermal wind (Dostalek, 2012). The areas surrounding Lidia are strongly influenced by the dynamical forcing induced by the trough and the jet streak in the P_{80} -ensemble (Fig. 8c and Fig. A3 in Appendix). It is worth noting that the QG ascent patterns near the TC center may partially reflect contributions from the TC's own circulation. This implies that some contamination from the TC's inner-core vorticity cannot be completely ruled out. To assess this, we performed an additional localized filtering applied exclusively to the TC circulation, which effectively removes most of the mesoscale contribution of the vortex. As shown in Appendix A3, the resulting Trenberth forcing field reveals a clearer synoptic-scale signal associated with the trough and the jet-streak interaction, supporting that the large-scale forcing dominates despite minor contamination near the TC center.

This result is further supported by the ERA5 reanalysis data (Fig. 8d), which reveals a Q pattern similar to that observed in the P_{80} -ensemble, but with greater intensity (note that ERA5 is only a member, not a composite group). In the absence of substantial thermodynamic differences (Figs. 2 and 3), these results highlight the dominant role of dynamic interaction between the trough, the jet streak, and the cyclone during RI. However, we acknowledge that tropospheric moisture, particularly the intrusion of mid-level dry air, may also have influenced the timing or suppression of RI in some members, as suggested by Fischer et al. (2023). These findings are particularly relevant for operational forecasting, also demonstrating the capability of the ECMWF EPS to simulate Lidia's RI, even under complex extratropical interactions influences.

The temporal evolution of the Trenberth forcing (Fig. 8e) reveals a clear and consistent signal in the P_{80} -ensemble, with significantly more negative values, indicative of stronger synoptic-scale upward motion. This enhanced forcing begins slightly before the onset of Lidia's RI (which starts around +55 h), with statistically significant differences emerging at approximately +50 h, and peaks between +50 and +70 h. This temporal analysis supports a causal interpretation, suggesting that the synoptic-scale dynamical forcing likely contributed to initiating the RI process, rather than being a consequence of it. In contrast, the P_{20} -ensemble shows much weaker and less coherent values throughout, indicating an absence of favorable dynamical support for RI.

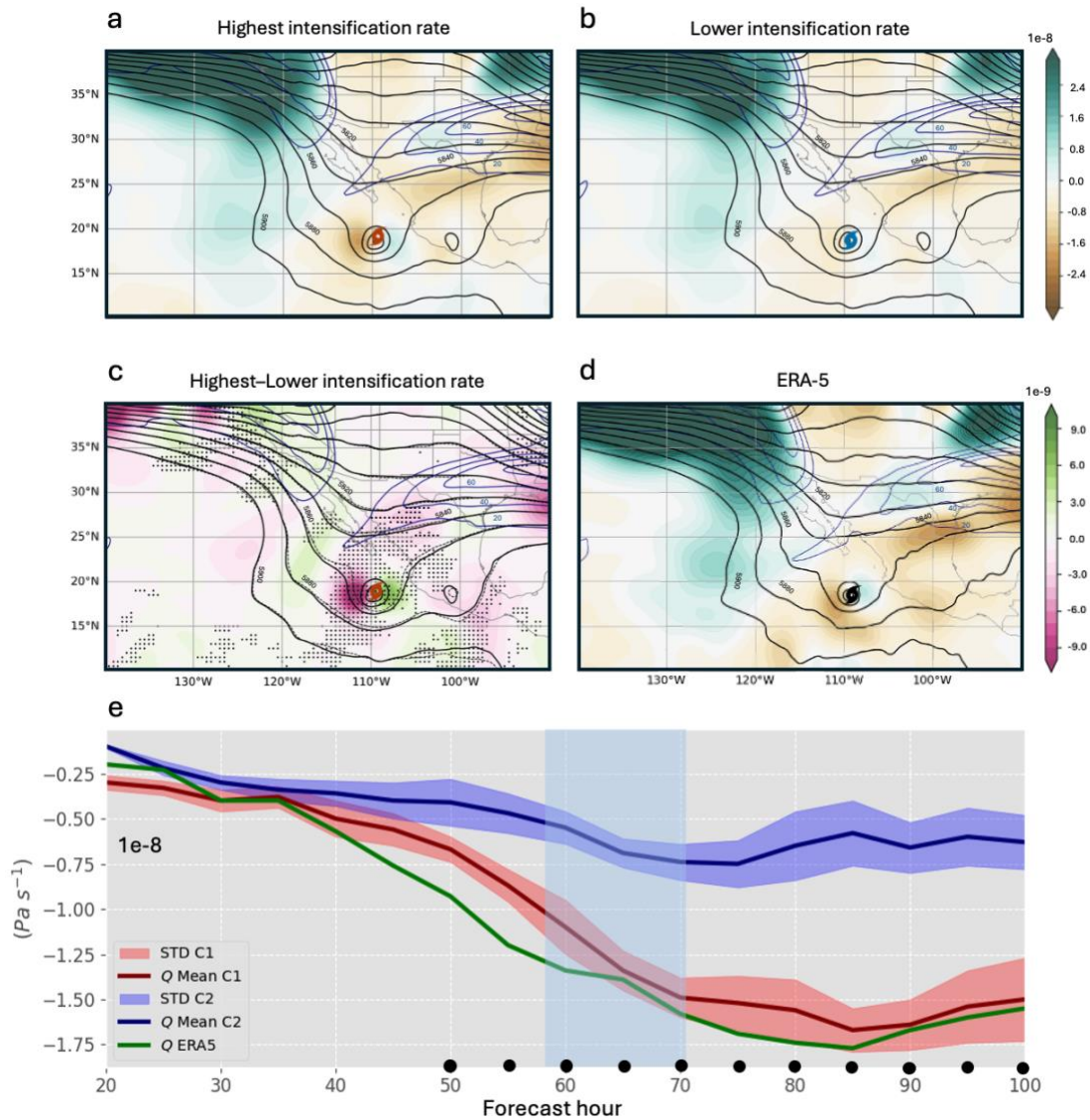


Figure 8. Q -Composite (shaded; $\text{Pa} \cdot \text{s}^{-1}$) at 500 hPa, jet stream (blue contours at 10 m s^{-1} intervals) at 250 hPa and Z at 500 hPa (black contours at 20 m intervals) of (a) the P_{80} (b) P_{20} IRG, (c) $P_{80} - P_{20}$ of Q (shaded; dots indicated statistical significance), solid (dashed) contour represent Z of P_{80} (P_{20}) IRG and (d) same for ERA5 data. (e) Q Temporal evolution calculated within a radial range of 500 km at 500 hPa, with the red (blue) line representing the higher (lower) IRG. The red (blue) shaded regions indicate the STD for the highest (lower) IRG and dots indicate statistical significance.

In P_{80} -ensemble, the trough is broader at Lidia's latitude, we found a difference of ≈ 300 km between the continuous and dashed contours and positioned closer to Lidia (around 500 km; Figs. 3a, b), in agreement with previous studies showing that favorable trough-TC interactions occur when the trough lies to the northwest at an optimal distance (Hanley et al., 2001). Significant differences are observed in both the amplitude and distance relative to Lidia (Fig. 2c). A similar pattern has been noted in some Atlantic basin cases (Hanley et al., 2001; Fischer et al., 2019; Sato et al., 2020), where effective trough-TC

interactions are facilitated by a favorable distance, typically between 500-1000 km. However, Fischer et al. (2019) found that northwestward-approaching troughs were associated with the lowest rates of RI among the configurations they examined, with stronger intensification occurring when a cutoff low was located to the southwest of the TC. While Lidia's interaction does not fully match this optimal configuration, the proximity and orientation of the trough in the RI group (Fig. 3a) still suggest a dynamically favorable setup, compared to the less aligned structure seen in the non-RI group (Fig. 3b). Although the TC itself may contribute to modifying the trough structure in the P_{80} -ensemble, it is noteworthy that a broader and deeper trough is already evident from the early forecast hours (see Fig. 4), suggesting a pre-existing synoptic configuration conducive to stronger TC–trough interaction.

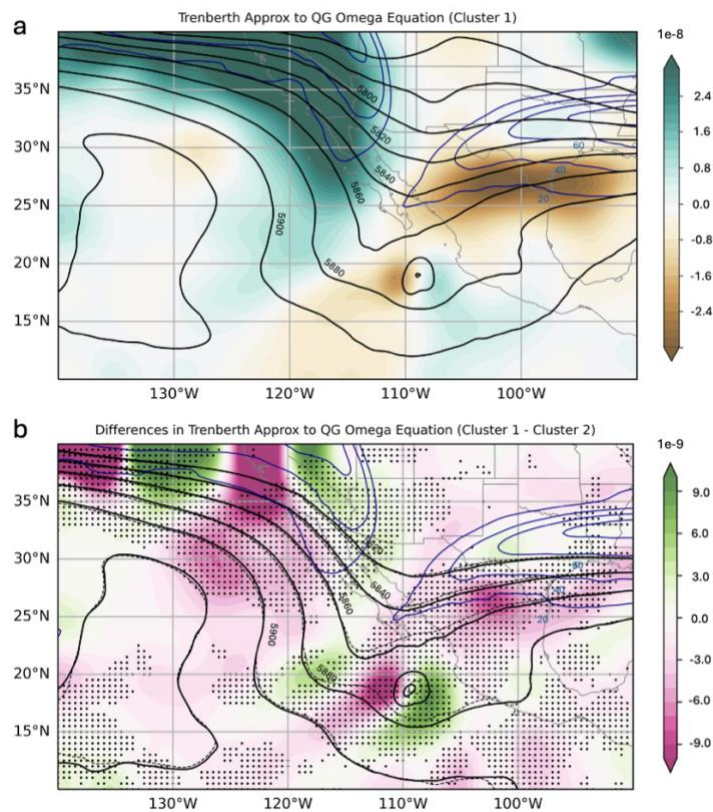


Figure 9. (a) Q -Composite (shaded; $Pa \cdot s^{-1}$) at 500 hPa, jet stream (blue contours at $10 m s^{-1}$ intervals) at 250 hPa and geopotential height at 500 hPa (black contours at 20 m intervals) of RI members, (b) Trenberth forcing (shaded) differences (P_{80} -RI members minus P_{20} ; dots indicated statistical significance), solid (dashed) contour represent geopotential height of RI group.

These findings further support the hypothesis that dynamical forcing triggered Lidia's RI. In the P_{80} -ensemble the trough is broader (~ 300 km) and closer to Lidia (~ 500 km; Figs. 10a, b). Evident differences are observed in both the amplitude and distance relative to Lidia (Fig. 10c). A similar configuration has been noted in some Atlantic basin cases (Hanley et al.,

2001; Fischer et al., 2019; Sato et al., 2020), where effective trough–TC interactions require a favorable distance. This configuration is associated with different behavior of \vec{V}_{irr} at upper-levels (Figs. 10d-f), where the proximity of the trough’s divergence zone enhances evacuation mass in the P_{80} -ensemble (Fig. 10d) with significant \vec{V}_{irr} differences reaching $\sim 4 \text{ ms}^{-1}$ to the west-northwest of Lidia. Consequently, the superposition of both divergence zones amplifies the upper-level anticyclonic circulation, consistent with increasing EFC values in P_{80} -ensemble toward Lidia (Fig. 5) strengthens upward motion and enabling RI.

On the other hand, the VWS remains moderate around Lidia’s center in both ensemble groups, with values between $10\text{-}15 \text{ ms}^{-1}$ during RI period (Fig. 10g, h). Slightly higher VWS values are observed to the south of Lidia. To the west and near of Lidia center, VWS values are higher in P_{80} -ensemble (around $\sim 5 \text{ ms}^{-1}$; Fig. 10i), though still within favorable ranges for intensification (Sharma and Varma, 2022). In contrast, regions beyond 2° radial distance in P_{80} -ensemble show significantly lower VWS values, consistent with the position and shape of the jet stream. In P_{20} -ensemble, a stronger jet stream is present north of Lidia, resulting in a more significant increase in VWS compared to P_{80} -ensemble. Thus, the position and intensity of the jet streak relative to Lidia’s position could potentially limit its intensification in P_{20} -ensemble.

The results suggest that the upward motions induced by dynamical mechanisms associated with Lidia’s interaction with a trough are consistent with the greater RH in P_{80} , particularly near the center of Lidia and in the southern region where the trough appears to enhance its influence (Figs. 10j–l). This region coincides with the trough-cyclone interaction, where vertical motions are strongly driven by dynamical forcing. Additional checks performed for forecast hours prior and during to RI already showed discernible differences in RH between both ensembles, with higher mid-tropospheric humidity in P_{80} -ensemble compared to the weak-intensifying members. The analyzed atmospheric patterns, including the dynamical forcing associated with the trough and jet streak, suggest that higher RH in P_{80} may be linked to increased condensation rates during air ascents around the center of Hurricane Lidia, leading to core warming (Emanuel, 1986; Zhang et al., 2013; Zhang and Emanuel, 2016). A moister mid-tropospheric environment can also suppress the intrusion of dry air, reduce ventilation and allow convection to remain deeper and more symmetric (Tang and Emanuel, 2010, 2012; Riemer et al., 2010; Ge et al., 2013). The enhanced latent heat release in such a moist environment strengthens the warm core and facilitates a greater and improved divergence in height, which facilitates the evacuation of mass from the core of the TC and favors a sustained ascent. This supports a more efficient upper-level outflow, effectively mitigating the detrimental influence of environmental VWS (Rios-Berrios and Torn, 2017; Qiu et al., 2020).

Specifically, the reduction in VWS observed in the P_{80} -ensemble reflects a weakening of the environmental vertical wind gradient over the storm core. This occurs as the interaction with the upper-level trough enhances mass divergence aloft, weakening the upper-level winds immediately above the cyclone. Simultaneously, stronger and more

vertically aligned convection, sustained by the higher mid-tropospheric humidity, reinforces the upper-level outflow and reorganizes the wind field around the vortex, effectively reducing the shear acting on the inner core (Riemer and Montgomery, 2011; Ge et al., 2013; Tang and Emanuel, 2012; Ryglicki et al., 2019). This process illustrates how the moist environment can offset the detrimental influence of environmental shear by reducing ventilation and enabling greater vertical mass flux within the TC core (Alland et al., 2021), rather than by promoting a more efficient coupling between the outflow and the ambient flow (Figs. 10g–l and Figs. 11c, d). Therefore, the observed reduction in shear is better understood as a localized, dynamically and thermodynamically mediated adjustment rather than a broad environmental change. Together, higher RH, reduced ventilation, and enhanced synoptic-scale forcing acted synergistically to precondition the vortex and create an optimal environment for rapid intensification in the P_{80} -ensemble.

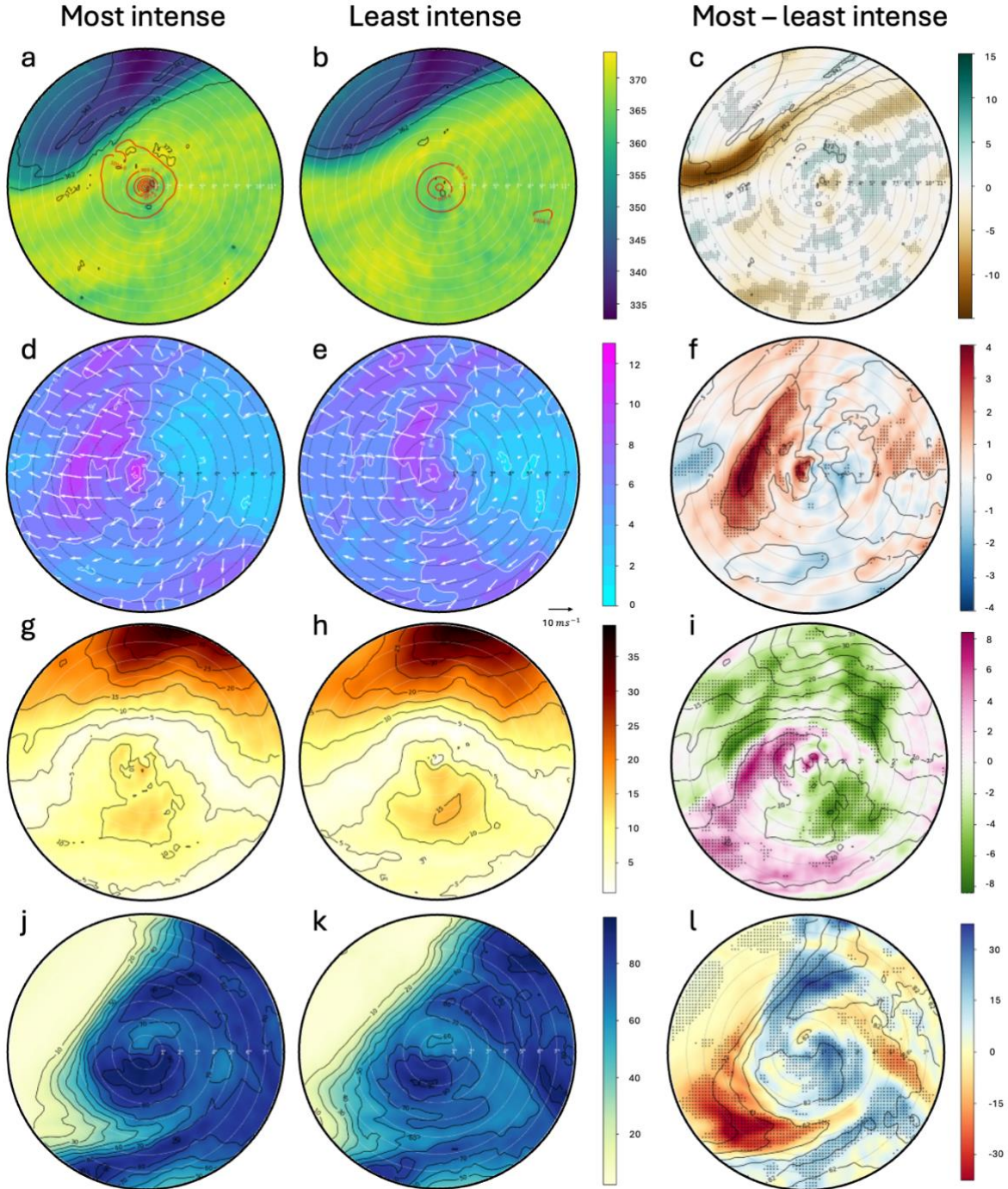


Figure 10. SCC for the time step 55-h of: θ (K) at 1.5 PVU for (a) P_{80} , (b) P_{20} IRG, and (c) $P_{80} - P_{20}$ IRG, red contours are MSPL; $|\vec{V}_{irr}|$ ($m s^{-1}$), at 200 hPa for (d) P_{80} , (e) P_{20} IRG, and (f) $P_{80} - P_{20}$ IRG; VWS ($m s^{-1}$; between 0-500 km radius) for (g) P_{80} , (h) P_{20} IRG and (i) $P_{80} - P_{20}$ IRG, and RH (%) (j) P_{80} , (k) P_{20} IRG and (l) $P_{80} - P_{20}$ IRG at 500 hPa. Each concentric ring in the panels corresponds to 1° radius, and the outermost circle representing the SCC domain has a radius of 8°

While the mean RH differences between the P_{80} - and P_{20} -ensembles were modest in magnitude, Figure 10I reveals statistically significant anomalies of approximately 10% near the storm center and along its southern flank. These regions of enhanced mid-tropospheric moisture likely played an active role in sustaining deep convection and facilitating the vertical alignment of the vortex, consistent with the stronger and more organized convective structure observed in the P_{80} -ensemble. This behavior is in agreement with previous studies (e.g., Alland et al., 2021; Tang and Emanuel, 2010), which demonstrated that higher mid-level humidity reduces ventilation and supports the maintenance of deep, symmetric convection even under moderate vertical wind shear.

Similarly, Hamaguchi and Takayabu (2021) described how upper-level dynamical forcing can induce synoptic-scale ascent that moistens the mid–upper troposphere prior to convective amplification in tropical disturbances. A comparable sequence is evident in the P_{80} -ensemble, where enhanced negative Trenberth forcing and upper-level divergence preceded a significant increase in mid-level relative humidity during the rapid intensification period (Fig. 11c, d). This correspondence reinforces the interpretation that upper-level dynamical ascent and mid-tropospheric moistening acted together to precondition the environment for RI in the P_{80} -ensemble.

Instead, the P_{80} -ensemble is characterized by early and sustained dynamic forcing, particularly the strong negative Trenberth forcing observed before the RI onset, which likely initiated upward motion and enhanced upper-level mass divergence near the storm core. This synoptic-scale ascent, coupled with the release of latent heat, contributed to a favorable adjustment of the potential vorticity structure in the upper troposphere, reinforcing the outflow and aiding in the vertical alignment of the vortex. Consequently, the observed reduction in VWS in P_{80} -ensemble can be interpreted as a combined result of both dynamic and thermodynamic processes acting in phase, rather than as a purely dynamical outcome. This reduction is related to higher Trenberth forcing, supporting a causal sequence in which synoptic-scale forcing preconditions, such as strong convection and vortex alignment, subsequently amplify this favorable state, accelerating the intensification process (Chen and Gopalakrishnan, 2019; Komaromi and Doyle, 2018; Stevenson et al., 2014). Figure 11 confirms this evolution: stronger divergence and PV anomalies emerge after the initial forcing, aligning with the onset of RI. The combined evidence supports the conclusion that in the case of Hurricane Lidia, RI was dynamically triggered by the interaction with the upper-level trough and jet stream, while thermodynamic factors such as PI, SST, and RH acted in concert with the dynamical forcing, serving as supportive components that enhanced the overall efficiency of the intensification process.

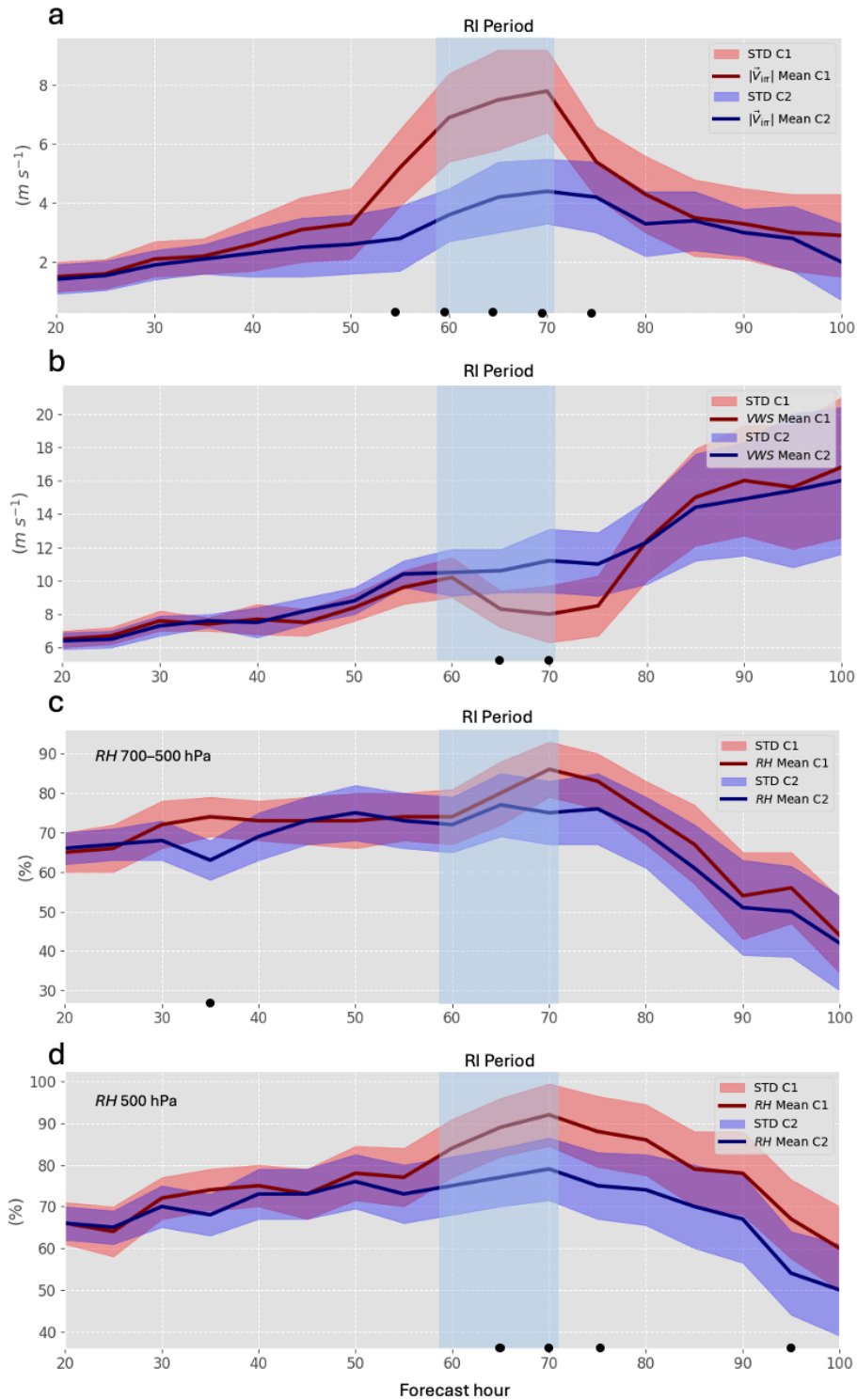


Figure 11. Time evolution of (a) ageostrophic wind at 250 hPa, (b) VWS (850–200 hPa), (c) RH (700–500 hPa) and (d) RH (500 hPa) within 500 km of Lidia. Red (blue) lines show the mean for the higher (lower) IRG; shaded areas indicate STD. Light blue band indicate the RI period. Black dots denote significant differences.

To better connect the individual diagnostics discussed in this study, Figure 12 presents a conceptual schematic summarizing the key mechanisms acting before, at the onset, and during Lidia’s RI. The illustration integrates the main results: (i) the approach and deformation of the upper-level trough, (ii) the strengthening of synoptic-scale ascent diagnosed through negative Trenberth forcing, (iii) the increase in upper-level divergence and cyclonic vorticity advection, (iv) the moistening of the mid-troposphere, and (v) the subsequent reduction of VWS and enhancement of the upper-level outflow. This schematic encapsulates how the combination of dynamic forcing and favorable thermodynamic conditions preconditioned and then accelerated the intensification process in the P_{80} -ensemble in this case of study.

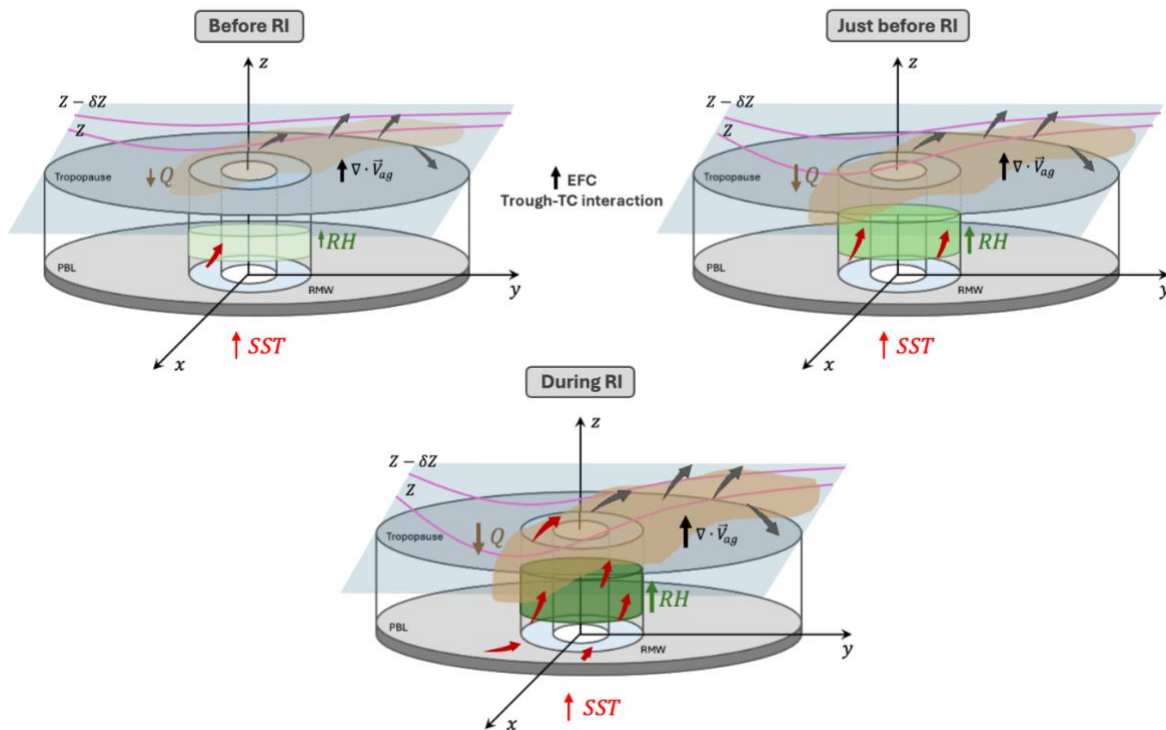


Figure 12. Schematic overview of the dynamical and thermodynamic processes leading to Hurricane Lidia’s RI. Before RI, the mid-level trough induces increasing dynamical forcing and weak ascent near the cyclone. Just before RI, enhanced negative Trenberth forcing (shaded region in brown) strengthens upper-level divergence (gray arrows) and mid-tropospheric moistening (light green cylinders). During RI, the interaction between the trough and the vortex maximizes ascent (red arrows), increases RH (green cylinder), and combines with elevated SST to support a deep, vertically aligned convective core.

4 Summary and conclusions

This research presents a novel examination of the interaction between a mid- and upper-level trough and Hurricane Lidia in the northeastern Pacific, a region where studies are less frequent compared to the Atlantic basin, particularly regarding RI. Since thermodynamic factors such as PI and SST do not seem to explain the differences observed

between the members of the group in the intensification of Lidia, some dynamic variables associated with forcings more typical of higher latitudes are analyzed, which usually appear in the autumn months in subtropical areas of the northeastern Pacific coasts (DiMego et al., 1976).

Based on previous work in the Atlantic basin (Fischer et al., 2019), which demonstrated that TCs experiencing RI often coincide with the presence of an upper-level trough approaching from the northwest at an optimal distance, our study expands this framework by demonstrating for the first time a similar dynamic configuration driving RI in the northeastern Pacific. By analyzing synoptic dynamical indicators, such as the Trenberth forcing, ageostrophic wind divergence and vorticity advection, we demonstrate how these dynamical processes play a crucial role in Lidia's RI. The EFC values greater than $10 \text{ ms}^{-1} \text{ day}^{-1}$ in the P_{80} -ensemble indicate the trough-TC interaction during the RI period, reinforcing the critical role of the trough in enhancing vertical motions and upper-level divergence. In a context where ocean temperatures are rising and an increasing trend in RI hurricane frequency has been documented (Majumdar et al., 2023; Li et al., 2023), this work provides the first case study of trough-TC interaction leading to RI in the northeastern Pacific, highlighting the increased proximity and breadth of the trough near Lidia a key driver of its RI. Unlike Fischer et al. (2019), who focused on climatological composites and individual case diagnostics in the Atlantic, this study provides a probabilistic ensemble-based assessment linked to dynamic forcings under realistic forecast uncertainty conditions.

The obtained results underscore the role of dynamical mechanisms, analyzed through quasi-geostrophic forcing, in triggering significant upward vertical motions that contribute to the Lidia's RI. These dynamics are evident in the P_{80} -ensemble (even more evident in RI members), where Lidia undergoes RI, showing stronger ageostrophic wind divergence, enhanced vorticity advection at mid- and upper-levels, and more pronounced Trenberth forcing, all associated with the influence of the trough (Fig. 12). In contrast, in the P_{20} -ensemble, the trough is still present but its interaction with Lidia appears less favorable, characterized by weaker dynamical coupling and a less optimal alignment between the trough axis and the cyclone center. The proximity and intensity of a jet stream to Lidia's north increase in VWS, which limited the potential for intensification.

The enhanced Trenberth forcing in the P_{80} -ensemble appears several hours before the onset of RI, indicating that synoptic-scale ascent likely preconditioned the environment rather than resulting from the intensification itself. This timing supports a causal interpretation in which the large-scale forcing drives changes within the TC. Following this initial dynamic trigger, latent heat release near the cyclone core contributed to a favorable upper-level PV redistribution. This adjustment likely enhanced the upper outflow layer and contributed to the subsequent reduction in VWS observed in the P_{80} group, further amplifying the intensification process.

On the other hand, although the mean relative humidity differences between the two ensembles were modest, a closer inspection revealed locally enhanced mid-tropospheric

moisture near the storm center and along the southern sector of Lidia, where the trough influence was strongest. This moisture distribution likely contributed to sustaining deep convection and mitigating mid-level ventilation of low-entropy air, allowing the vortex to remain vertically aligned and more resistant to environmental shear (Riemer and Montgomery, 2011; Tang and Emanuel, 2012; Ge et al., 2013). Therefore, while the synoptic-scale dynamic forcing acted as the primary trigger for upward motion and potential vorticity redistribution, the accompanying moist environment played a complementary role by enhancing latent heat release and reducing the effective VWS over the cyclone core. In this sense, RH acted not merely as a passive background condition but as a cooperative thermodynamic factor that amplified the impact of the dynamic forcing, ultimately supporting the RI observed in the P_{80} -ensemble.

By demonstrating the effectiveness of EPS-ECMWF in capturing complex trough-TC interactions, this study highlights the critical role of EPS as an indispensable tool for operational forecasting in the northeastern Pacific, especially along the Pacific coast of Mexico. EPS are particularly valuable for quantifying uncertainty in RI scenarios, which remain challenging to predict due to the complex dynamical and thermodynamical processes involved. The present results show that EPS can successfully differentiate between dynamically favorable and unfavorable environments, even in a context where high-resolution operational models are not readily available, as is often the case in Mexico. This makes EPS-based diagnostics especially useful for forecasters operating in data-sparse or resource-limited settings. In this region, during autumn months, the subtropical jet stream frequently interacts with TCs, increasing the likelihood of dynamical forcing mechanisms that can either enhance or inhibit intensification.

This study illustrates how broader and deeper mid-level troughs, such as the one observed at 500 hPa in Hurricane Lidia, can significantly enhance vertical motion and upper-level divergence conducive to RI. Operationally, diagnostic tools such as Trenberth forcing and EFC metric could be integrated into forecasting to better assess trough-TC interactions. Measuring these variables in real time would provide forecasters with actionable insights into the likelihood of RI, particularly when TCs recurve toward the densely populated Pacific coast of Mexico. Although the limitations of a single case study are evident, we suspect that other RIs in the northeastern Pacific have been influenced by similar dynamical mechanisms. However, while our results offer robust evidence from a synoptic-scale perspective, this study is based on a single case. Future research should expand this methodology to a broader set of events and explore complementary approaches using convection-permitting high-resolution simulations. Such simulations would help resolve inner-core processes and mesoscale interactions that were intentionally simplified in this study, which focused on evaluating large-scale dynamical forcings. In this regard, the framework proposed here serves as a cost-effective, scalable strategy to support RI forecasting in regions with limited access to high-resolution modeling systems and highlights the continued need to refine multi-scale diagnostic techniques for better understanding and prediction of TC intensification. Also, expanding this methodology to a broader set of cases

could offer a more comprehensive understanding of trough-TC interactions and their role in RI, ultimately improving operational forecasting capabilities in this understudied region.

Appendix

To complement and further clarify the dynamical interpretation presented in the main manuscript, this Appendix provides three additional diagnostic figures that illustrate key synoptic features relevant to Lidia's RI. Figure A1 documents the evolution of the upper-tropospheric jet stream, offering temporal context for the intensifying trough-TC interaction. Figure A2 shows geopotential height anomalies from ERA5, highlighting the anomalous large-scale environment in which the RI occurred. Figure A3 presents the filtered Trenberth forcing fields used to isolate the synoptic-scale contribution to vertical motion, demonstrating that the main dynamical signals identified in the P_{80} -ensemble persist even after suppressing the TC's inner-core circulation. Together, these supplementary diagnostics reinforce the robustness of the mechanisms discussed in the main text and provide additional transparency regarding the interpretation of the ensemble-based results.

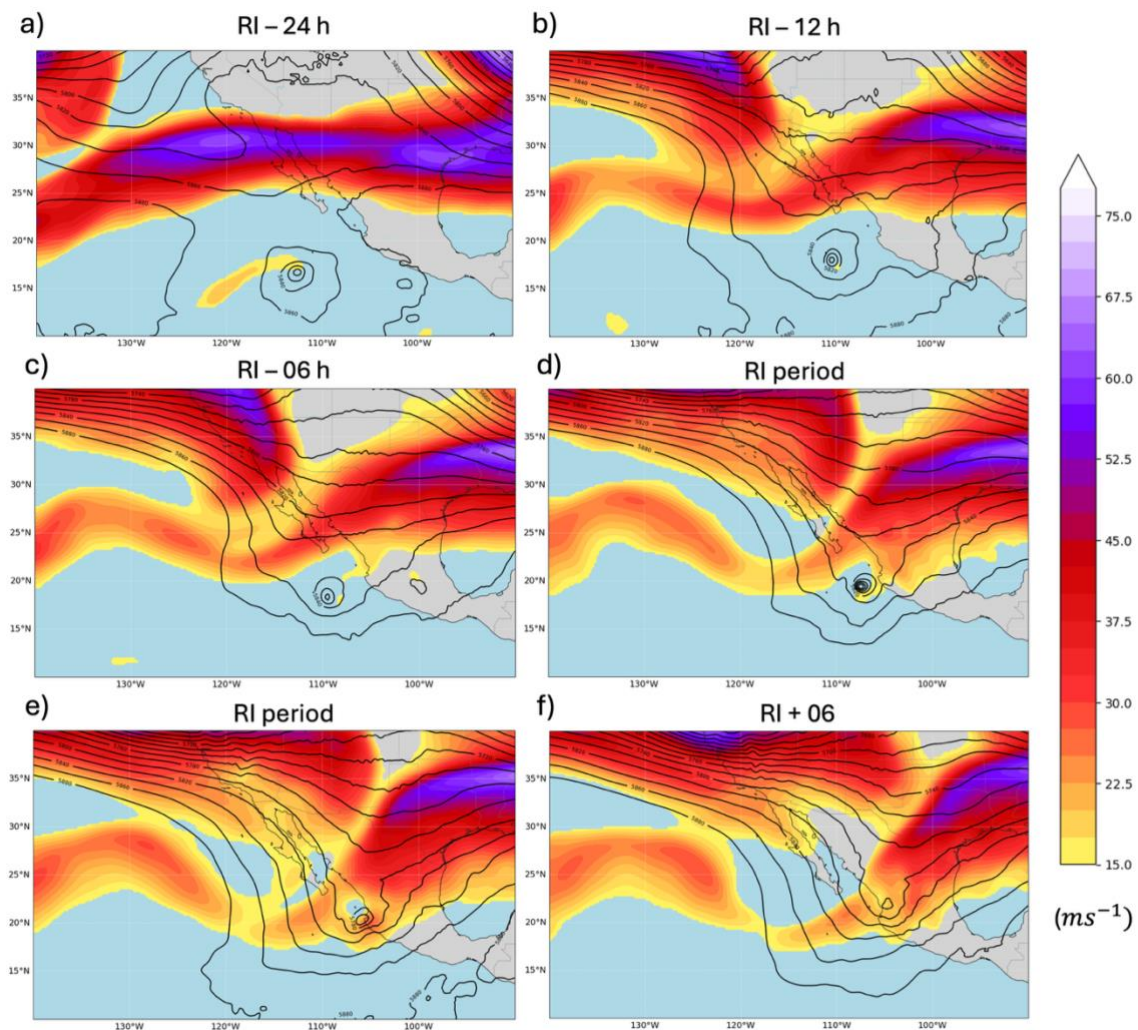


Figure A1. Upper-tropospheric jet stream before, during and after RI of Hurricane Lidia at 250 hPa. Shaded colors denote wind speed (ms^{-1}), highlighting the jet stream core, while black contours represent geopotential height (gpm) at 500 hPa. Panels show consecutive time steps relative to the onset of RI: (a) -24 h, (b) -12 h, (c) -06 h, (d) onset RI period, (e) RI period, and (f) +06 h.

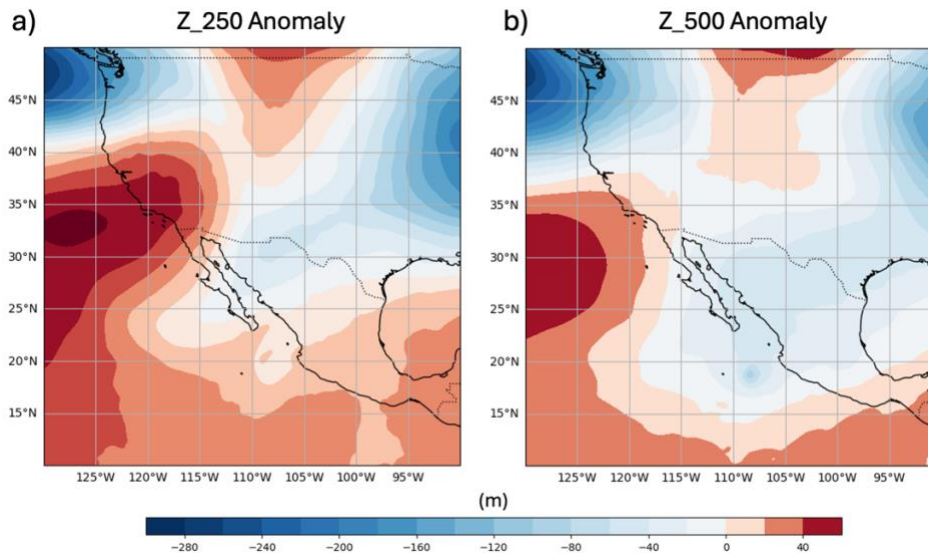


Figure A2. Z anomalies from ERA5 for (a) 250 and (b) 500 hPa during the period surrounding Lidia's RI (12:00 UTC on 9 October, 2023). Warm (red) shading denotes positive height anomalies, while cool (blue) shading indicates negative anomalies.

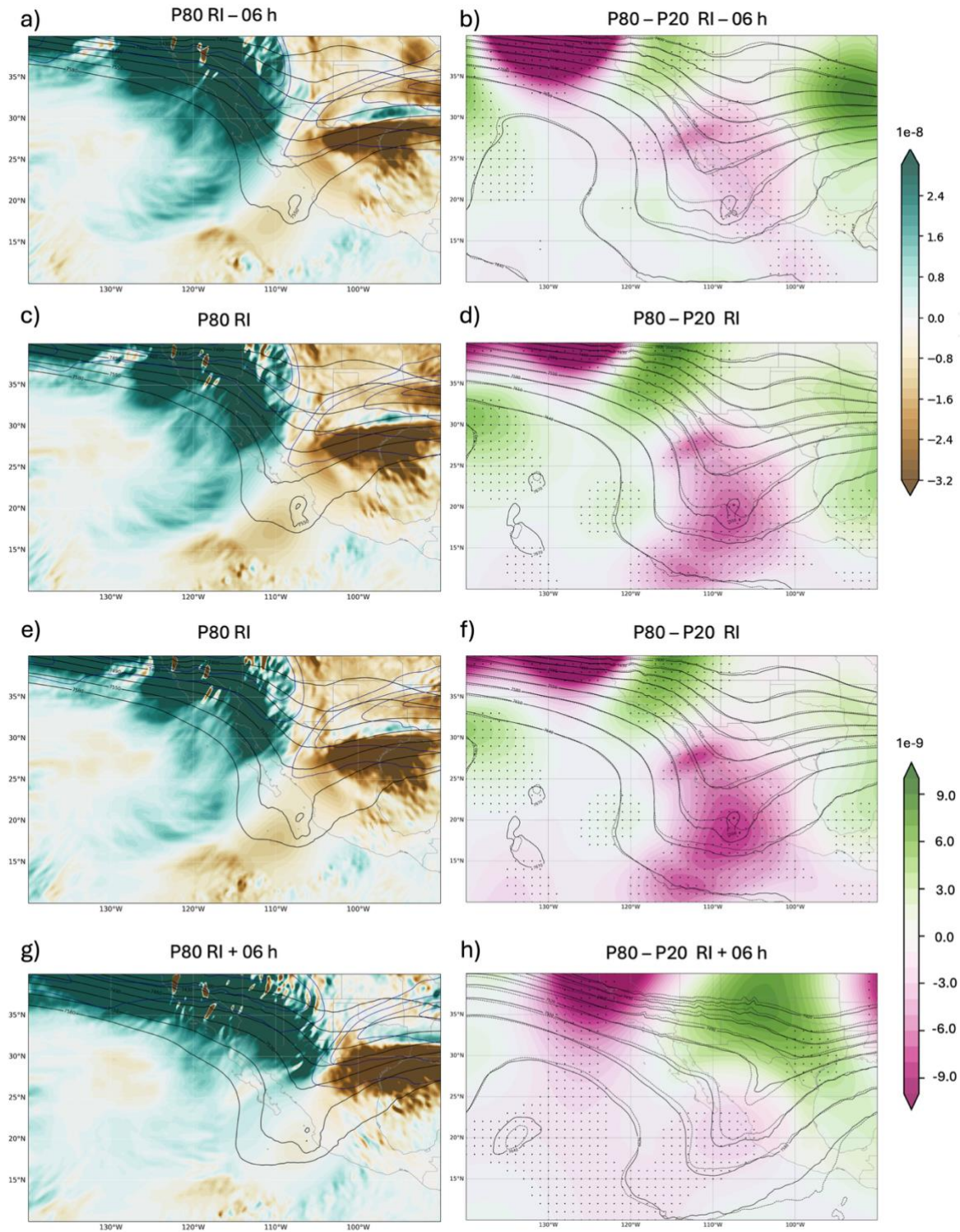


Figure A3. (a, c, e, g) Filtered Trenberth forcing fields for the P_{80} -ensemble (left column) at selected times relative to the RI onset (-06 h, RI, $+06$ h). A Gaussian storm-centered filter ($\sigma = 2.5^\circ$ with a gradual taper of $\sigma = 1^\circ$) is applied to suppress the TC's inner-core circulation while retaining the synoptic-scale signal. Shading shows the filtered Trenberth forcing, and

black contours denote Z at 500-hPa. (b, d, f, h) Shading represents the $P_{80} - P_{20}$ of Trenberth forcing, with contours showing the corresponding 500-hPa height fields from each ensemble. Dots indicate grid points where the differences are statistically significant.

Declaration of Competing Interest

The authors declare no conflicts of interest relevant to this study.

Acknowledgments

This work was partially supported by the research project PID2023-146344OB-I00 (CONSCIENCE) financed by MICIU/AEI /10.13039/501100011033 and by FEDER, UE, and the two ECMWF Special Projects (SPESMART and SPESVALE). Thanks to the reviewers of this paper for their valuable comments. Mauricio López-Reyes extends his sincere gratitude to the Institute of IAM of the University of Guadalajara and Instituto Frontera A.C., for his invaluable support. C. Calvo-Sancho acknowledges the grant awarded by the Spanish Ministry of Science and Innovation - FPI program (PRE2020-092343), and acknowledges support from the GVA. PROMETEO Grant CIPROM/2023/38; and CSIC-LINCGLOBAL Ref. LINCG24042. J.J. González-Alemán thanks support from the Spanish State Meteorological Agency.

Open Research

The tracking data for Hurricane Lidia can be found in López-Reyes, M. (2024). Atmospheric data sets can be accessed through the MARS database, hosted by ECMWF, at <https://confluence.ecmwf.int/display/MARS>. Additionally, ERA-5 reanalysis data base is allowed in Climate Data Store (CDS; available at <https://climate.copernicus.eu/climate-reanalysis>).

Author contributions

Conceptualization: MLR, MLMP, JJGA. Methodology: MLR, MLMP, CCS, JJGA. Project administration: MLMP. Supervision: MLPM, CCS, JJGA. Writing-original draft: MLR. Writing-review and edits: MLR, MLMP, CCS, JJGA.

References

Alland, J. J., Tang, B. H., Corbosiero, K. L., and Bryan, G. H.: Combined effects of midlevel dry air and vertical wind shear on tropical cyclone development. Part I: Downdraft ventilation, *J. Atmos. Sci.*, 78, 763–782, <https://doi.org/10.1175/JAS-D-20-0054.1>, 2021a.

Alland, J. J., Tang, B. H., Corbosiero, K. L., and Bryan, G. H.: Combined effects of midlevel dry air and vertical wind shear on tropical cyclone development. Part II: Radial ventilation, *J. Atmos. Sci.*, 78, 783–796, <https://doi.org/10.1175/JAS-D-20-0055.1>, 2021b.

Avila, L. A.: Forecasting tropical cyclone intensity changes: An operational challenge, Preprints, Symp. on Tropical Cyclone Intensity Change, Phoenix, AZ, Amer. Meteor. Soc., 1–3, 1998.

Billingsley, D.: A review of QG theory—Part III: A different approach, *Natl. Wea. Dig.*, 22, 3–10, 1998.

Bister, M. and Emanuel, K. A.: Dissipative heating and hurricane intensity, *Meteor. Atmos. Phys.*, 65, 233–240, <https://doi.org/10.1007/BF01030791>, 1998.

Bister, M. and Emanuel, K. A.: Low frequency variability of tropical cyclone potential intensity 1. Interannual to interdecadal variability, *J. Geophys. Res.-Atmos.*, 107, ACL-26, <https://doi.org/10.1029/2001JD000776>, 2002.

Bluestein, H. B.: *Synoptic-dynamic meteorology in midlatitudes: Observations and theory of weather systems*, Vol. 2, Taylor & Francis, 1992.

Bracken, W. E. and Bosart, L. F.: The role of synoptic-scale flow during tropical cyclogenesis over the North Atlantic Ocean, *Mon. Weather Rev.*, 128, 353–376, [https://doi.org/10.1175/1520-0493\(2000\)128<0353:TROSSF>2.0.CO;2](https://doi.org/10.1175/1520-0493(2000)128<0353:TROSSF>2.0.CO;2), 2000.

Braun, S. A. and Tao, W.-K.: Sensitivity of high-resolution simulations of Hurricane Bob (1991) to planetary boundary layer parameterizations, *Mon. Weather Rev.*, 128, 3941–3961, [https://doi.org/10.1175/1520-0493\(2000\)129<3941:SOHRSO>2.0.CO;2](https://doi.org/10.1175/1520-0493(2000)129<3941:SOHRSO>2.0.CO;2), 2000.

Callaghan, J.: WITHDRAWN: The interaction of Hurricane Michael with an upper trough leading to intensification right up to landfall, *Trop. Cyclone Res. Rev.*, 9, 135–142, <https://doi.org/10.1016/j.tccr.2019.07.009>, 2020.

Cangialosi, J. P.: The state of hurricane forecasting, National Hurricane Center Blog—Inside the Eye, <https://noaanhc.wordpress.com/2018/03/09/the-state-of-hurricaneforecasting>, 2018.

Cao, J., Ran, L., and Li, N.: An application of the Helmholtz theorem in extracting the externally induced deformation field from the total wind field in a limited domain, *Mon. Weather Rev.*, 142, 2060–2066, <https://doi.org/10.1175/MWR-D-13-00311.1>, 2014.

Carrasco, C., Landsea, C., and Lin, Y.: The influence of tropical cyclone size on its intensification, *Weather Forecast.*, 29, 582–590, <https://doi.org/10.1175/WAF-D-13-00092.1>, 2014.

Chen, H. and Gopalakrishnan, S. G.: A study on the asymmetric rapid intensification of Hurricane Earl (2010) using the HWRF system, *J. Atmos. Sci.*, 72, 531–550, <https://doi.org/10.1175/JAS-D-14-0097.1>, 2015.

Chen, X., Zhang, J. A., and Marks, F. D.: A thermodynamic pathway leading to rapid intensification of tropical cyclones in shear, *Geophys. Res. Lett.*, 46, 9241–9251, <https://doi.org/10.1029/2019GL083667>, 2019.

Chen, Y., Gao, S., Li, X., and Shen, X.: Key environmental factors for rapid intensification of the South China Sea tropical cyclones, *Front. Earth Sci.*, 8, 609727, <https://doi.org/10.3389/feart.2020.609727>, 2021.

Collins, C., Hesser, T., Rogowski, P., and Merrifield, S.: Altimeter observations of tropical cyclone-generated sea states: Spatial analysis and operational hindcast evaluation, *J. Mar. Sci. Eng.*, 9, 216, <https://doi.org/10.3390/jmse9020216>, 2021.

DeMaria, M., Kaplan, J., and Baik, J.: Upper-level eddy angular momentum fluxes and tropical cyclone intensity change, *J. Atmos. Sci.*, 50, 1133–1147, [https://doi.org/10.1175/1520-0469\(1993\)050<1133:ULEAMF>2.0.CO;2](https://doi.org/10.1175/1520-0469(1993)050<1133:ULEAMF>2.0.CO;2), 1993.

DeMaria, M., Franklin, J. L., Onderlinde, M. J., and Kaplan, J.: Operational forecasting of tropical cyclone rapid intensification at the National Hurricane Center, *Atmosphere*, 12, 683, <https://doi.org/10.3390/atmos12060683>, 2021.

DiMego, G. J., Bosart, L. F., and Endersen, G. W.: An examination of the frequency and mean conditions surrounding frontal incursions into the Gulf of Mexico and Caribbean Sea, *Mon. Weather Rev.*, 104, 709–718, [https://doi.org/10.1175/1520-0493\(1976\)104<0709:AEOTFA>2.0.CO;2](https://doi.org/10.1175/1520-0493(1976)104<0709:AEOTFA>2.0.CO;2), 1976.

Dostalek, J. F., Schubert, W., DeMaria, M., Estep, D., Johnson, R., and Vonder Haar, T.: Global omega equation: Derivation and application to tropical cyclogenesis in the North Atlantic Ocean, 2012.

Emanuel, K. A.: An air-sea interaction theory for tropical cyclones. Part I: Steady-state maintenance, *J. Atmos. Sci.*, 43, 585–605, [https://doi.org/10.1175/1520-0469\(1986\)043<0585:AASITF>2.0.CO;2](https://doi.org/10.1175/1520-0469(1986)043<0585:AASITF>2.0.CO;2), 1986.

Emanuel, K. A.: The maximum intensity of hurricanes, *J. Atmos. Sci.*, 45, 1143–1155, [https://doi.org/10.1175/1520-0469\(1988\)045<1143:tmioh>2.0.co;2](https://doi.org/10.1175/1520-0469(1988)045<1143:tmioh>2.0.co;2), 1988.

Emanuel, K. A. and Lin, J.: Hurricane Otis: A case for a rapid migration toward probabilistic tropical cyclone forecasting, 36th Conference on Hurricanes and Tropical Meteorology, American Meteorological Society, 2024.

Fischer, M. S.: Tropical cyclone rapid intensification in environments of upper-tropospheric troughs: Environmental influences and convective characteristics, PhD thesis, ProQuest One Academic (Order No. 10839442), 2018.

Fischer, M. S., Tang, B. H., and Corbosiero, K. L.: A climatological analysis of tropical cyclone rapid intensification in environments of upper-tropospheric troughs, *Mon. Weather Rev.*, 147, 3693–3719, <https://doi.org/10.1175/MWR-D-19-0013.1>, 2019.

Fischer, M. S., Reasor, P. D., Tang, B. H., Corbosiero, K. L., Torn, R. D., and Chen, X.: A tale of two vortex evolutions: Using a high-resolution ensemble to assess the impacts of ventilation on a tropical cyclone rapid intensification event, *Mon. Weather Rev.*, 151, 297–320, <https://doi.org/10.1175/MWR-D-22-0037.1>, 2023.

García-Franco, J. L., Gómez-Ramos, O., and Domínguez, C.: Hurricane Otis: The costliest and strongest hurricane at landfall on record in Mexico, *Weather*, 79, 182–184, <https://doi.org/10.1002/wea.4555>, 2024.

Ge, X., Li, T., and Peng, M.: Effects of vertical shears and midlevel dry air on tropical cyclone developments, *J. Atmos. Sci.*, 70, 3859–3875, <https://doi.org/10.1175/JAS-D-13-066.1>, 2013.

Gilford, D. M.: pyPI (v1.3): Tropical cyclone potential intensity calculations in Python, *Geosci. Model Dev.*, 14, 2351–2369, <https://doi.org/10.5194/gmd-14-2351-2021>, 2021.

Hanley, D., Molinari, J., and Keyser, D.: A composite study of the interactions between tropical cyclones and upper-tropospheric troughs, *Mon. Weather Rev.*, 129, 2570–2584, [https://doi.org/10.1175/1520-0493\(2001\)129<2570:ACSOTI>2.0.CO;2](https://doi.org/10.1175/1520-0493(2001)129<2570:ACSOTI>2.0.CO;2), 2001.

Heming, J. T., Prates, F., Bender, M. A., Bowyer, R., Cangialosi, J., Caroff, P., and Xiao, Y.: Review of recent progress in tropical cyclone track forecasting and expression of uncertainties, *Trop. Cyclone Res. Rev.*, 8, 181–218, <https://doi.org/10.1016/j.tcr.2020.01.001>, 2019.

Hersbach, H., Bell, B., Berrisford, P., Hirahara, S., Horányi, A., Muñoz-Sabater, J., and Thépaut, J. N.: The ERA5 global reanalysis, *Q. J. Roy. Meteor. Soc.*, 146, 1999–2049, <https://doi.org/10.1002/qj.3803>, 2020.

Hu, Y. and Zou, X.: Tropical cyclone center positioning using single channel microwave satellite observations of brightness temperature, *Remote Sens.*, 13, 2466, <https://doi.org/10.3390/rs13132466>, 2021.

Jin, R., Li, Y., Chen, X., and Li, M.: Characteristics of the upper-level outflow and its impact on the rapid intensification of Typhoon Roke (2011), *Front. Earth Sci.*, 10, 1021308, <https://doi.org/10.3389/feart.2022.1021308>, 2023.

Kaplan, J. and DeMaria, M.: Large-scale characteristics of rapidly intensifying tropical cyclones in the North Atlantic basin, *Weather Forecast.*, 18, 1093–1108, [https://doi.org/10.1175/1520-0434\(2003\)018<1093:LCORIT>2.0.CO;2](https://doi.org/10.1175/1520-0434(2003)018<1093:LCORIT>2.0.CO;2), 2003.

Komaromi, W. A. and Doyle, J. D.: On the dynamics of tropical cyclone and trough interactions, *J. Atmos. Sci.*, 75, 2687–2709, <https://doi.org/10.1175/JAS-D-17-0272.1>, 2018.

Larson, J., Zhou, Y., and Higgins, R. W.: Characteristics of landfalling tropical cyclones in the United States and Mexico: Climatology and interannual variability, *J. Climate*, 18, 1247–1262, <https://doi.org/10.1175/JCLI3317.1>, 2005.

Leroux, M., Plu, M., and Roux, F.: On the sensitivity of tropical cyclone intensification under upper-level trough forcing, *Mon. Weather Rev.*, 144, 1179–1202, <https://doi.org/10.1175/MWR-D-15-0224.1>, 2016.

Ling, S., Lu, R., and Cao, J.: The variation in tropical cyclone genesis over the western North Pacific during the El Niño summers, *Clim. Dynam.*, 63, 13, <https://doi.org/10.1007/s00382-024-07484-9>, 2025.

Liu, T., Liu, Z., Zhao, Y., and Zhang, S.: Strong extratropical impact on observed ENSO, *J. Climate*, 37, 943–962, <https://doi.org/10.1175/JCLI-D-23-0023.1>, 2024.

López-Reyes, M. and Meulenert, A.: Comparación de las variables físicas que influyen en la rápida intensificación de los ciclones tropicales del Océano Pacífico nororiental durante el periodo 1970–2018, *Cuad. Geogr.*, 60, 105–125, <https://doi.org/10.30827/cuadgeo.v60i2.15474>, 2021.

López-Reyes, M.: Lidia's tracking, Zenodo [data set], <https://doi.org/10.5281/zenodo.14187335>, 2024a.

López-Reyes, M., González-Alemán, J. J., Calvo-Sancho, C., Bolgiani, P., Sastre, M., and Martín, M. L.: Remote interactions between tropical cyclones: The case of Hurricane Michael and Leslie's high predictability uncertainty, *Atmos. Res.*, 107697, <https://doi.org/10.1016/j.atmosres.2024.107697>, 2024b.

Loughe, A. F., Lai, C., and Keyser, D.: A technique for diagnosing three-dimensional ageostrophic circulations in baroclinic disturbances on limited-area domains, *Mon. Weather Rev.*, 123, 1476–1504, [https://doi.org/10.1175/1520-0493\(1995\)123<1476:ATFDTD>2.0.CO;2](https://doi.org/10.1175/1520-0493(1995)123<1476:ATFDTD>2.0.CO;2), 1995.

Luna-Niño, R., Cavazos, T., Torres-Alavez, J. A., Giorgi, F., and Coppola, E.: Interannual variability of the boreal winter subtropical jet stream and teleconnections over the CORDEX-

CAM domain during 1980–2010, *Clim. Dynam.*, 57, 1571–1594, <https://doi.org/10.1007/s00382-020-05509-7>, 2021.

Mann, H. B. and Whitney, D. R.: On a test of whether one of two random variables is stochastically larger than the other, *Ann. Math. Stat.*, 18, 50–60, [enlace sospechoso eliminado], 1947.

Molinari, J. and Vollaro, D.: External influences on hurricane intensity. Part II: Vertical structure and response of the hurricane vortex, *J. Atmos. Sci.*, 47, 1902–1918, [https://doi.org/10.1175/1520-0469\(1990\)047<1902:EIOHIP>2.0.CO;2](https://doi.org/10.1175/1520-0469(1990)047<1902:EIOHIP>2.0.CO;2), 1990.

Montgomery, M. T. and Smith, R. K.: Comments on “Marathon versus sprint: Two modes of tropical cyclone rapid intensification in a global convection-permitting simulation”, *Mon. Weather Rev.*, 153, 365–367, <https://doi.org/10.1175/MWR-D-24-0029.1>, 2025.

Pasch, R. J.: Hurricane Milton Discussion Number 12, National Hurricane Center, 2024a.

Pasch, R. J.: Tropical Cyclone Report: Hurricane Lidia (EP152023), National Hurricane Center, https://www.nhc.noaa.gov/data/tcr/EP152023_Lidia.pdf, 2024b.

Peirano, C. M., Corbosiero, K. L., and Tang, B. H.: Revisiting trough interactions and tropical cyclone intensity change, *Geophys. Res. Lett.*, 43, 5509–5515, <https://doi.org/10.1002/2016GL069040>, 2016.

Prasanth, S., Chavas, D. R., Marks Jr., F. D., Dubey, S., Shreevastava, A., and Krishnamurti, T. N.: Characterizing the energetics of vortex-scale and sub-vortex-scale asymmetries during tropical cyclone rapid intensity changes, *J. Atmos. Sci.*, 77, 315–336, <https://doi.org/10.1175/JAS-D-19-0067.1>, 2020.

RAMMB/CIRA Slider: GOES-16 visible satellite image, <https://rammb-slider.cira.colostate.edu/>, 2024.

Riemer, M. and Montgomery, M. T.: Simple kinematic models for the environmental interaction of tropical cyclones in vertical wind shear, *Atmos. Chem. Phys.*, 11, 9395–9414, <https://doi.org/10.5194/acp-11-9395-2011>, 2011.

Ríos-Berríos, R., Torn, R. D., and Davis, C. A.: A closer look at the structure and intensity changes of rapidly intensifying tropical cyclones, *Mon. Weather Rev.*, 146, 3625–3645, <https://doi.org/10.1175/MWR-D-18-0111.1>, 2018.

Rygllicki, D. R., Doyle, J. D., Hodyss, D., Cossuth, J. H., Jin, Y., Viner, K. C., and Schmidt, J. M.: The unexpected rapid intensification of tropical cyclones in moderate vertical wind shear. Part III: Outflow–environment interaction, *Mon. Weather Rev.*, 147, 2919–2940, <https://doi.org/10.1175/MWR-D-18-0370.1>, 2019.

Ryglicki, D. R., Velden, C. S., Reasor, P. D., Hodyss, D., and Doyle, J. D.: Observations of atypical rapid intensification characteristics in Hurricane Dorian (2019), *Mon. Weather Rev.*, 149, 2131–2150, <https://doi.org/10.1175/MWR-D-20-0413.1>, 2021.

Sadler, J.: The upper tropospheric circulation over the global tropics, University of Hawaii, <https://www.soest.hawaii.edu/Library/Sadler.html>, 1975.

Sato, K., Inoue, J., and Yamazaki, A.: Performance of forecasts of hurricanes with and without upper-level troughs over the mid-latitudes, *Atmosphere*, 11, 702, <https://doi.org/10.3390/atmos11070702>, 2020.

Servicio Meteorológico Nacional: Special bulletin: Hurricane Otis rapid intensification and landfall warning, Comisión Nacional del Agua (CONAGUA), Mexico, <https://smn.cna.gob.mx/tools/DATA/Ciclones%20Tropicales/Resumenes/2023.pdf>, 2023.

Sharma, N. and Varma, A. K.: Impact of vertical wind shear in modulating tropical cyclones eye and rainfall structure, *Nat. Hazards*, 112, 2083–2100, <https://doi.org/10.1007/s11069-022-05257-3>, 2022.

Shi, D. and Chen, G.: The implication of outflow structure for the rapid intensification of tropical cyclones under vertical wind shear, *Mon. Weather Rev.*, 149, 4107–4127, <https://doi.org/10.1175/MWR-D-21-0141.1>, 2021.

Shi, D. and Chen, G.: Modulation of asymmetric inner-core convection on midlevel ventilation leading up to the rapid intensification of Typhoon Lekima (2019), *J. Geophys. Res.-Atmos.*, 128, e2022JD037952, <https://doi.org/10.1029/2022JD037952>, 2023.

Smith, R. K., Kilroy, G., and Montgomery, M. T.: Tropical cyclone life cycle in a three-dimensional numerical simulation, *Q. J. Roy. Meteor. Soc.*, 147, 3373–3393, <https://doi.org/10.1002/qj.4133>, 2021.

Stevenson, S. N., Corbosiero, K. L., and Molinari, J.: The convective evolution and rapid intensification of Hurricane Earl (2010), *Mon. Weather Rev.*, 142, 4364–4380, <https://doi.org/10.1175/MWR-D-14-00078.1>, 2014.

Tan, Z. M., Lei, L., Wang, Y., Xu, Y., and Zhang, Y.: Typhoon track, intensity, and structure: From theory to prediction, *Adv. Atmos. Sci.*, 39, 1789–1799, <https://doi.org/10.1007/s00376-022-2212-1>, 2022.

Tang, B. and Emanuel, K.: Midlevel ventilation's constraint on tropical cyclone intensity, *J. Atmos. Sci.*, 67, 1817–1830, <https://doi.org/10.1175/2010JAS3318.1>, 2010.

Tang, B. and Emanuel, K.: A ventilation index for tropical cyclones, *Bull. Amer. Meteor. Soc.*, 93, 1901–1912, <https://doi.org/10.1175/BAMS-D-11-00165.1>, 2012.

Tao, D., Van Leeuwen, P. J., Bell, M., and Ying, Y.: Dynamics and predictability of tropical cyclone rapid intensification in ensemble simulations of Hurricane Patricia (2015), *J. Geophys. Res.-Atmos.*, 127, e2021JD036079, <https://doi.org/10.1029/2021JD036079>, 2022.

Tong, B., Wang, X., Wang, D., and Zhou, W.: A novel mechanism for extreme El Niño events: Interactions between tropical cyclones in the western North Pacific and sea surface warming in the eastern tropical Pacific, *J. Climate*, 36, 2585–2601, <https://doi.org/10.1175/JCLI-D-21-1014.1>, 2023.

Wang, Y., Li, Y., Xu, J., Tan, Z. M., and Lin, Y.: The intensity dependence of tropical cyclone intensification rate in a simplified energetically based dynamical system model, *J. Atmos. Sci.*, 78, 2033–2045, <https://doi.org/10.1175/JAS-D-20-0393.1>, 2021.

Winters, A. C. and Attard, H. E.: North Pacific and North Atlantic jet covariability and its relationship to cool season temperature and precipitation extremes, *Weather Forecast.*, 37, 1581–1600, <https://doi.org/10.1175/WAF-D-21-0203.1>, 2022.

Wu, L., Su, H., Fovell, R. G., Dunkerton, T. J., Wang, Z., and Kahn, B. H.: Impact of environmental moisture on tropical cyclone intensification, *Atmos. Chem. Phys.*, 15, 14041–14053, <https://doi.org/10.5194/acp-15-14041-2015>, 2015.

Zhang, D. L. and Chen, H.: Importance of the upper-level warm core in the rapid intensification of a tropical cyclone, *Geophys. Res. Lett.*, 39, <https://doi.org/10.1029/2011GL050578>, 2012.

Zhang, J. A., Rogers, R. F., Reasor, P. D., Uhlhorn, E. W., and Marks Jr., F. D.: Asymmetric hurricane boundary layer structure from dropsonde composites in relation to the environmental vertical wind shear, *Mon. Weather Rev.*, 141, 3968–3984, <https://doi.org/10.1175/MWR-D-12-00335.1>, 2013.

Zhang, F. and Emanuel, K.: On the role of surface fluxes and WISHE in tropical cyclone intensification, *J. Atmos. Sci.*, 73, 2011–2019, <https://doi.org/10.1175/JAS-D-16-0011>, 2016.

Zhao, H. and Raga, G. B.: On the distinct interannual variability of tropical cyclone activity over the eastern North Pacific, *Atmósfera*, 28, 161–178, <https://doi.org/10.20937/ATM.2015.28.03.02>, 2015.